Geophysical Journal International

Geophys. J. Int. (2020) **222,** 412–435
Advance Access publication 2020 April 11
GJI Seismology

doi: 10.1093/gji/ggaa171

Full wave sensitivity of *SK*(*K*)*S* phases to arbitrary anisotropy in the upper and lower mantle

Andrea Tesoniero,[1] Kuangdai Leng,[1,2] Maureen D. Long[1] and Tarje Nissen-Meyer[2]

[1]*Department of Geology and Geophysics, Yale University, 210 Whitney Avenue, New Haven, CT 06520, USA. E-mail: andrea.tesoniero@yale.edu*
[2]*Department of Earth Sciences, University of Oxford, South Parks Road, Oxford OX13AN, UK*

Accepted 2020 April 1. Received 2020 April 1; in original form 2019 August 29

SUMMARY

Core-refracted phases such as *SKS* and *SKKS* are commonly used to probe seismic anisotropy in the upper and lowermost portions of the Earth's mantle. Measurements of *SK*(*K*)*S* splitting are often interpreted in the context of ray theory, and their frequency dependent sensitivity to anisotropy remains imperfectly understood, particularly for anisotropy in the lowermost mantle. The goal of this work is to obtain constraints on the frequency dependent sensitivity of *SK*(*K*)*S* phases to mantle anisotropy, particularly at the base of the mantle, through global wavefield simulations. We present results from a new numerical approach to modelling the effects of seismic anisotropy of arbitrary geometry on seismic wave propagation in global 3-D earth models using the spectral element solver AxiSEM3D. While previous versions of AxiSEM3D were capable of handling radially anisotropic input models, here we take advantage of the ability of the solver to handle the full fourth-order elasticity tensor, with 21 independent coefficients. We take advantage of the computational efficiency of the method to compute wavefields at the relatively short periods (5 s) that are needed to simulate *SK*(*K*)*S* phases. We benchmark the code for simple, single-layer anisotropic models by measuring the splitting (via both the splitting intensity and the traditional splitting parameters ϕ and δt) of synthetic waveforms and comparing them to well-understood analytical solutions. We then carry out a series of numerical experiments for laterally homogeneous upper mantle anisotropic models with different symmetry classes, and compare the splitting of synthetic waveforms to predictions from ray theory. We next investigate the full wave sensitivity of *SK*(*K*)*S* phases to lowermost mantle anisotropy, using elasticity models based on crystallographic preferred orientation of bridgmanite and post-perovskite. We find that *SK*(*K*)*S* phases have significant sensitivity to anisotropy at the base of the mantle, and while ray theoretical approximations capture the first-order aspects of the splitting behaviour, full wavefield simulations will allow for more accurate modelling of *SK*(*K*)*S* splitting data, particularly in the presence of lateral heterogeneity. Lastly, we present a cross-verification test of AxiSEM3D against the SPECFEM3D_GLOBE spectral element solver for global seismic waves in an anisotropic earth model that includes both radial and azimuthal anisotropy. A nearly perfect agreement is achieved, with a significantly lower computational cost for AxiSEM3D. Our results highlight the capability of AxiSEM3D to handle arbitrary anisotropy geometries and its potential for future studies aimed at unraveling the details of anisotropy at the base of the mantle.

Key words: Planetary interiors; Numerical modelling; Computational seismology; Seismic anisotropy; Wave propagation.

1 INTRODUCTION

Seismic anisotropy, the property of elastic materials to manifest directionally dependent seismic wave speeds (e.g. Anderson 1989; Babuska & Cara 1991), occurs in many regions of the Earth, including the crust (e.g. Barruol & Kern 1996), the upper mantle (e.g. Silver 1996; Savage 1999), the transition zone (e.g. Foley & Long 2011; Yuan & Beghein 2013), the uppermost lower mantle (e.g. Lynner & Long 2015; Ferreira *et al.* 2019), the D'' region at the base of the mantle (e.g. Nowacki *et al.* 2011; Creasy *et al.* 2017) and the inner core (e.g. Beghein & Trampert 2003). Because mantle anisotropy reflects deformation processes, knowledge of its presence, style and strength yields insight into past and present mantle flow (e.g. Long & Becker 2010). The proper characterization of seismic anisotropy is therefore crucial for our understanding of the dynamics of Earth's mantle. Our ability to completely characterize anisotropy in the mantle is limited, however, in part due to limitations imposed by seismic data coverage, and in part due to theoretical or computational limitations to relate observations to Earth structure. It is common in many global seismological studies to either neglect anisotropy entirely, and consider an isotropic approximation to Earth structure, or to consider only simple anisotropic geometries, such as radial anisotropy.

Elastic anisotropy manifests itself in the seismic wavefield in many ways, including the difference in propagation velocity between vertically polarized Rayleigh waves and horizontally polarized Love waves (e.g. Anderson 1961; Moulik & Ekström 2014), the splitting of normal modes (e.g. Anderson & Dziewonski 1982; Tromp 1995; Beghein *et al.* 2008), the directional dependence of traveltimes of body waves such as P_n (e.g. Hess 1964; Buehler & Shearer 2017) or surface waves (e.g. Forsyth 1975; Schaeffer *et al.* 2016), the scattering of energy from Love waves to Rayleigh waves via the coupling of spheroidal and toroidal modes (e.g. Park & Yu 1993; Servali *et al.* 2020), the polarization of *P* waves (e.g. Schulte-Pelkum *et al.* 2001) and directionally dependent *P*-to-*S* conversions as manifested in receiver functions (e.g. Levin & Park 1998; Wirth & Long 2014). The most widely used technique for detecting anisotropy in the mantle, however, is shear wave splitting or birefringence (e.g. Silver 1996; Savage 1999; Long & Silver 2009). The splitting of *SKS* and *SKKS* phases is routinely measured to study anisotropy in both the upper mantle (e.g. Silver & Chan 1991; Wolfe & Silver 1998; Levin *et al.* 1999; Long & van der Hilst 2005; Long 2013; Roy *et al.* 2014) and in the lowermost mantle (e.g. Niu & Perez 2004; Restivo & Helffrich 2006; Long 2009; Roy *et al.* 2014; Long & Lynner 2015; Grund & Ritter 2018; Reiss *et al.* 2019). Core traversing phases such as *SKS* and *SKKS* have several distinct advantages for shear wave splitting analysis. These include the known initial polarization of the shear wave, controlled by the *P*-to-*S* conversion at the core–mantle boundary (CMB), the lack of source-side effects, and the ability to observe clear *SK*(*K*)*S* phases that are often easily identifiable on seismograms. Shear wave splitting analysis also has several shortcomings, however; chief among these is the lack of vertical resolution of anisotropy, since it is a path-integrated measurement, and the need to obtain splitting measurements from multiple azimuths in order to fully characterize the anisotropic structure.

While a full 21 elastic parameters are needed to fully describe arbitrary anisotropy, it is common to use simpler parametrizations of anisotropy that invoke assumptions about anisotropic symmetry. For example, in global tomographic inversions that include radial anisotropy, under the assumption of hexagonal symmetry (e.g. Auer *et al.* 2014; Tesoniero *et al.* 2015), it is typical to use 5 parameters to describe the model, rather than the 2 needed for the isotropic case (e.g. Ritsema *et al.* 2011). Similarly, inversions of *SKS* splitting data for azimuthal anisotropy in the upper mantle typically rely on reduced parametrizations (e.g. Monteiller & Chevrot 2011; Lin *et al.* 2014a; Mondal & Long 2019). While such parametrizations may make sense in the context of practical limitations on observational data sets, they may not always be realistic for actual Earth materials. For example, olivine, the primary mineral constituent of the upper mantle and the major cause of upper mantle anisotropy, has orthorhombic symmetry, although deformed olivine aggregates may be approximated with higher symmetry classes (e.g. Karato *et al.* 2008). In any case, it is desirable to have computational tools that can simulate accurate wave propagation through anisotropic media of arbitrary symmetry efficiently; furthermore, azimuthal anisotropy is a well-known property of the upper mantle, so it is necessary for wavefield modelling schemes to be able to handle azimuthal anisotropy in addition to the more commonly invoked radial anisotropy.

Measurements of shear wave splitting are commonly interpreted in the framework of ray theory, either implicitly or explicitly. The most straightforward interpretation of *SKS* splitting measurements, for example, invokes a single layer of azimuthal anisotropy beneath a station whose properties (symmetry axis orientation, strength of anisotropy and/or layer thickness) are related to the observed splitting parameters (typically fast splitting direction, ϕ and delay time, δt) via a simple ray theoretical approximation. In some cases, complex patterns of *SKS* splitting, in which apparent splitting parameters vary with backazimuth, are interpreted as reflecting multiple layers of anisotropy (e.g. Marson-Pidgeon & Savage 2004; Eakin & Long 2013), via analytical equations that were developed based on a ray theoretical approximation (Silver & Savage 1994). While there has been some work on the nature of the frequency dependent sensitivity of *SKS* phases to upper mantle anisotropy (e.g. Favier & Chevrot 2003; Favier *et al.* 2004; Chevrot 2006; Long *et al.* 2008; Sieminski *et al.* 2008; Lin *et al.* 2014a; Mondal & Long 2019), only a few observational studies have actually used finite-frequency sensitivity estimates to interpret (or invert) actual data (Monteiller & Chevrot 2011; Lin *et al.* 2014b). Furthermore, the finite-frequency sensitivity of *SKS* and *SKKS* phases to anisotropy in the lowermost mantle remains poorly understood. Given the increasing use of *SK*(*K*)*S* phases in studies of deep mantle anisotropy, it is crucial to understand the nature of this sensitivity.

For both upper and lowermost mantle anisotropy studies, it is desirable to have a computationally efficient tool to simulate global seismic wave propagation for *SK*(*K*)*S* phases in anisotropic media with arbitrary symmetry. The popular spectral-element based community software package SPECFEM3D_GLOBE (Komatitsch & Tromp 2002a,b) is capable of handling arbitrary anisotropy, but its significant computational requirements make global simulations at the periods relevant for *SK*(*K*)*S* phases (down to ∼5–10 s) impractical. In this study, we make use of the AxiSEM3D code (Leng *et al.* 2016, 2019), a coupled pseudospectral spectral element solver for 3-D global wavefield propagation in realistic 3-D earth models. While previously released versions of AxiSEM3D only handled radially anisotropic input models, the actual solver is capable of handling the full fourth-order elasticity tensor C_{ijkl} with 21 independent coefficients. We have modified the formulation of the input models to handle arbitrary elasticity, and in this study we test and implement a range of anisotropic mantle models that include azimuthal anisotropy, relevant for *SK*(*K*)*S* splitting. The AxiSEM3D code combines the advantages of a full 3-D spectral element method to model complex, 3-D structures with the computational efficiency of axisymmetric methods; this allows the user to model complex and realistic Earth structures with significant computational speedup and without significant loss of performance (Leng *et al.* 2019).

The goal of this study is to evaluate the frequency dependent effects of anisotropy of different symmetry classes (albeit in relatively simple, laterally homogeneous structures) on the splitting of *SK*(*K*)*S* phases, via global wavefield simulations for seismic periods down 5 s. We generate synthetic seismograms for a suite of earth models with anisotropy in the upper and lowermost mantle, and analyse the synthetic *SKS* and *SKKS* waveforms by measuring shear wave splitting using both the traditional transverse component energy minimization method (Silver & Chan 1988) and the splitting intensity method (Chevrot 2000). We present benchmark results for simple cases, including one based on the spherically symmetric PREM model (Dziewonski & Anderson 1981) and one that invokes vertically propagating shear waves travelling through a transverse isotropic medium with a horizontal axis of symmetry (HTI). We then model global wave propagation for more realistic upper mantle anisotropy scenarios, including approximations to olivine crystallographic preferred orientation (CPO) that invoke both hexagonal and orthorhombic symmetry. Next, we investigate the effects of anisotropy in the D'' layer at the base of the mantle on *SK*(*K*)*S* splitting, via a series of global wavefield simulations for models that invoke CPO of lower mantle minerals such as bridgmanite and post-perovskite. In the last part we provide a verification of our implementation of full anisotropy via a benchmark solution against the full 3-D spectral element solver SPECFEM3D_GLOBE. We then discuss the implications of our results from relatively simple models for future work on the interpretation of shear wave splitting measurements in terms of mantle anisotropy, particularly as more complex models are considered.

2 ANISOTROPIC MODELLING STRATEGY WITH AxiSEM3D

AxiSEM3D (Leng *et al.* 2016, 2019) is a powerful hybrid spectral element solver for 3-D global wave propagation in realistic Earth structures. It aims to bridge the gap between computationally expensive simulation methods for 3-D Earth structure and faster simulation methods for spherically symmetric earth models. It is a fully convergent 3-D method not unlike other discrete full 3-D methods, for example SPECFEM3D_GLOBE. The method follows the axisymmetric spectral element solver AxiSEM which assumes spherically symmetric or axisymmetric structures. To accommodate arbitrary 3-D structures, AxiSEM3D is built upon a collection of coupled axisymmetric 2-D domains. This relies on the fact that wavefields in realistic 3-D structures are relatively smooth in the azimuthal direction (Leng *et al.* 2016), and can thus be accurately represented in the azimuthal direction by honouring this smooth complexity rather than a complexity-blind, fine discretization just as in the in-plane dimension or for conventional 3-D methods. AxiSEM3D couples the azimuthal dimension by Fourier series, which can assume arbitrarily low or high expansion orders for each patch in the source-receiver plane. This hybrid formulation combines the strength of a full 3-D discrete method to compute global wavefields with the significant speedup of computational time of 2-D methods. In other words, a 3-D global wavefield in complex earth models can be efficiently computed at a cost that scales almost as (multiple) 2-D simulations, allowing us to run simulations of global wavefield propagation over a large frequency range with relatively limited computer resources. This computational efficiency is coupled with the capability of AxiSEM3D to readily allow the usage of 3-D earth models based on global tomography, including those available from the Incorporated Research Institutions for Seismology (IRIS) Earth Model Collaboration (EMC) in netCDF format. Independent modules can be invoked to handle certain geometrical properties, such as surface topography or topography on boundaries such as the CMB (Leng *et al.* 2019). AxiSEM3D automatically handles radial anisotropy if the velocity structure of the underlying seismic velocity model is provided as horizontal and vertical compressional and shear wave velocity values. Detailed descriptions of the theoretical formulation of AxiSEM3D and benchmark tests with independent, fully 3-D discrete spectral element solvers (e.g. SPECFEM3D_GLOBE) are given in (Leng *et al.* 2016, 2019).

For this study, we take advantage of the accuracy and efficiency of the method to solve the elastodynamic wave equation in global media, and implement a new independent module which introduces general anisotropy of arbitrary symmetry. The mathematical formulation of the three-dimensional wave equation is based on the generalized Hooke's law, $\sigma_{ij} = C_{ijkl}\varepsilon_{kl}$,which relates the components of the stress tensor σ_{ij} to the strain tensor ε_{kl} through the fourth-order elasticity tensor C_{ijkl}. The elasticity tensor describes the elastic properties of the material, and in the most general case it can be fully described by 21 independent coefficients (see Malvern 1969; Babuska & Cara 1991,for details). In the new anisotropic module, the elastic properties of a specific anisotropic region in the domain are described by 21 independent elastic parameters, as opposed to the 2 Lamé constants (λ and μ) for the isotropic case or the 5 Love parameters (A, C, L, N, F, described further below) for the vertical transverse isotropy (VTI) case. In order to use the general anisotropy module in AxiSEM3D, the user must provide the solver with a netCDF file containing the information about the elasticity tensor and the anisotropic media's geographical location within the model domain.

Introducing general anisotropy (an intrinsically 3-D property of the medium) usually only accounts for a relatively small increment of the total computational cost. However, similarly to the case for lateral heterogeneity in (isotropic) velocity structure, the user must ensure that the Fourier degree of expansion is larger than the size of the heterogeneous structure, in order to ensure a correct representation of the seismic wavefield. Moreover, the user must take particular caution in taking into account the geometrical properties of the elasticity tensor. This is usually defined in a local coordinate system such that certain crystallographic axes (or a strain directions) align certain geographic coordinates. However, AxiSEM3D works with a global spherical coordinate system. Therefore, except at the geographical poles (where the coordinate systems coincide), a rotation matrix must be applied to the elasticity tensor (specified by the user in a local coordinate system) to translate its orientation to the global domain of AxiSEM3D.

3 BENCHMARK TESTS FOR SIMPLE ANISOTROPIC MODELS

We begin by running two different numerical tests with the intention to benchmark the new anisotropic module of AxiSEM3D against well-understood wave propagation behaviour for simple anisotropic models. In the first of these, we run a global wavefield simulation for the 1-D PREM model (Dziewonski & Anderson 1981), which includes radial anisotropy in the depth range between 25 and 220 km depth. In the second of these, we run wave propagation simulations for a simple, single layer of anisotropy with a horizontal axis of transverse isotropy (HTI), reproducing a synthetic test presented in Chevrot (2000).

3.1 Radially anisotropic PREM

In the first test, we run global wavefield simulations for PREM under two different conditions:

(1) using the traditional model input format of AxiSEM3D, in which radial anisotropy is specified via horizontal and vertical velocity values for both *P* and *S* waves and

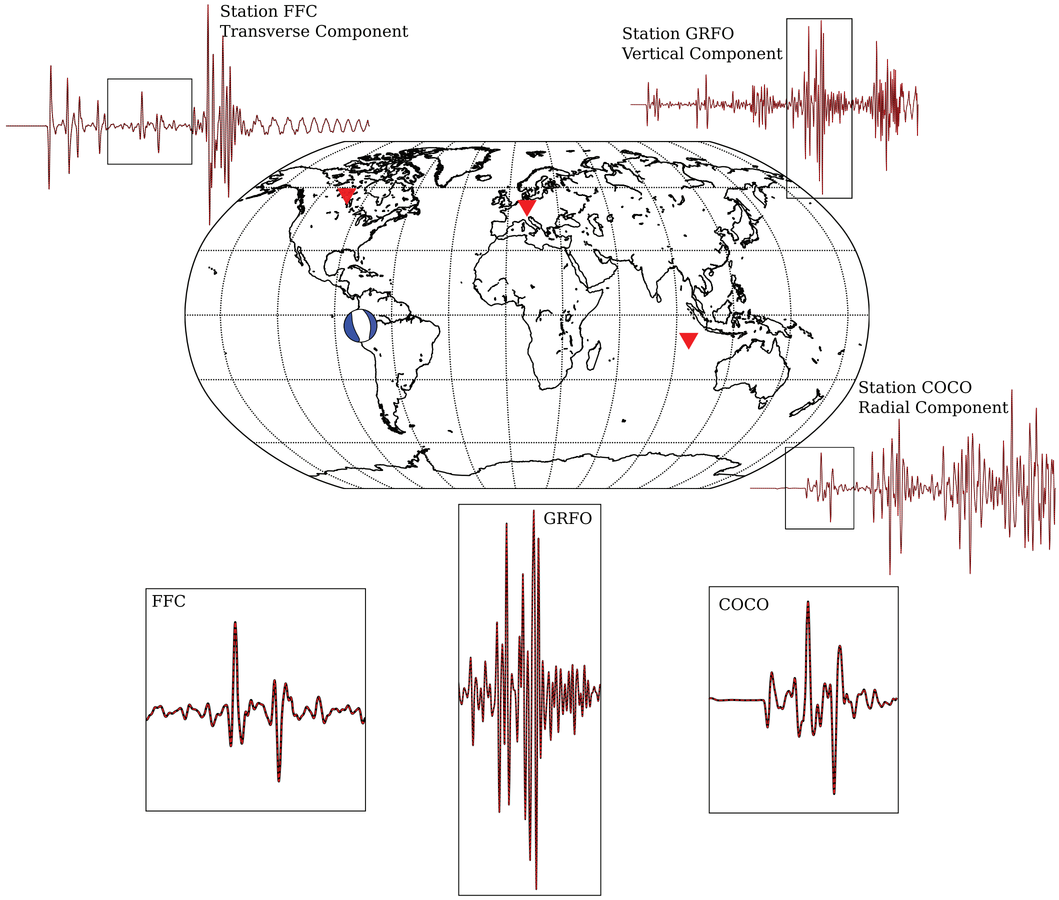

Figure 1. Map showing the source–receiver configuration settings and the synthetic results for the self-benchmarking tests computed using AxiSEM3D with the anisotropic PREM model (black seismograms) and the solution obtained using a description of the anisotropic PREM as C_{ijkl} (red seismograms). Three representative pairs of synthetic seismograms are plotted at three different locations. A close-up view of the synthetics is shown in the three boxes at the bottom of the figures for three different sections of the time-series.

(2) using the model input format of the new anisotropy module, in which anisotropy is specified via the full elasticity tensor.

This allows us to test whether we have correctly implemented the specification of elasticity in the new module, and whether we have correctly implemented the tensor rotations needed to map the local coordinate system of the model input file to the global spherical coordinate system of AxiSEM3D. In order to parametrize the PREM model in the new input file, we replace the elastic constants in the depth range between 24 and 220 km with equivalent elastic coefficients of the 6 × 6 elasticity tensor that describes the radial anisotropy contained in anisotropic PREM. At other depths, we use the isotropic PREM values, which are specified via the Lamé constants λ, μ (and the density ρ). The relationship between the full elasticity tensor C_{ijkl} and the Love parameters that describe radial anisotropy are given by the following relationships (e.g. Babuska & Cara 1991):

$$
\begin{aligned}
A &= \rho {V_{PH}}^2\\
C &= \rho {V_{PV}}^2\\
L &= \rho {V_{SV}}^2\\
N &= \rho {V_{SH}}^2\\
F &= \eta(A - 2L)
\end{aligned}
\tag{1}
$$

$$
C_{ijkl} = \begin{pmatrix}
A & A-2N & F & \cdot & \cdot & \cdot\\
A-2N & A & F & \cdot & \cdot & \cdot\\
F & F & C & \cdot & \cdot & \cdot\\
\cdot & \cdot & \cdot & L & \cdot & \cdot\\
\cdot & \cdot & \cdot & \cdot & L & \cdot\\
\cdot & \cdot & \cdot & \cdot & \cdot & N
\end{pmatrix}
\tag{2}
$$

with A, C, L, N being the parameters associated to the horizontal and vertical compressional and shear seismic wave speed and F being the parameter associated to seismic waves propagating in intermediate directions through the coefficient η. We run the simulation for a hypothetical earthquake in the South American subduction zone whose moment tensor is represented by the focal mechanism in Fig. 1, which also shows the two sets of synthetic seismograms for different components at three representative stations (FFC, GRFO and COCO). This test shows the general ability of our new anisotropy module to correctly specify the full elasticity tensor for models that include radial anisotropy; however, this test is not capable of capturing the effects that azimuthally dependent anisotropy have on the propagating wavefield.

3.2 Single anisotropic layer with vertical wave propagation

In order to test whether the new anisotropy model correctly represents the effects of azimuthal anisotropy for simple models, we

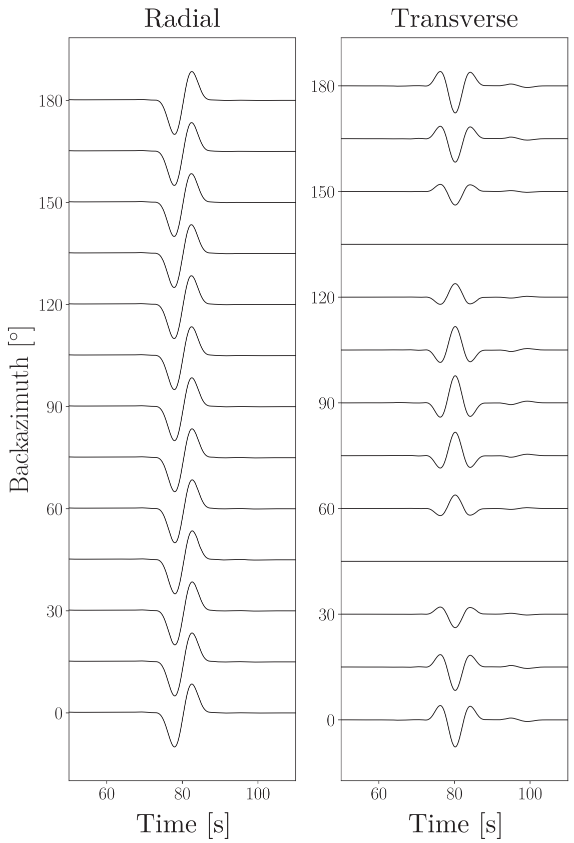

Figure 2. Synthetic seismograms computed for a vertically propagating shear wave in a 30-km-thick horizontally transverse isotropic (HTI) layer with 3 per cent anisotropy. The amplitude of the transverse component is amplified by a factor of 10.

carry out a second benchmarking exercise modelled on a synthetic test presented in Chevrot (2000). We consider wave propagation through a single layer of anisotropy of thickness 30 km, with a horizontal axis of transversely isotropic symmetry (HTI) at an azimuth of 45° North. The strength of anisotropy in the layer is 3 per cent, and the value of the parameter η is 1.03. We use a density of 2450 kg m^{-3} along with an average P-wave velocity of 6.50 km s^{-1} and an S-wave velocity of 3.75 km s^{-1} for the anisotropic layer. In order to mimic the synthetic test of Chevrot (2000) closely, and to avoid global waveform effects, we use a point source sitting directly beneath the receiver, just beneath the anisotropic layer to induce perfectly vertical S-wave propagation. We use a monopole point source that radiates energy entirely polarized in a single direction, and consider different polarization directions of the source in order to explore the azimuthal dependence of the waveforms. To properly define the backazimuth, we set both source and receiver located along the same vertical direction, with the source slightly shifted along the latitudinal direction by 0.01°. This minor deviation does not substantially affect the polarization of the seismic energy which will remain confined in a single direction. As an alternative approach, we also tested a scheme that keeps source and receiver perfectly assigned and instead rotates the elasticity tensor by 15° for each simulation. Both approaches deliver the same results. We designate the horizontal component parallel to the initial polarization direction of the S wave as the radial component, and examine how the behaviour of the transverse component varies with azimuth (following Chevrot 2000). We convolve the synthetic seismograms with a Gaussian source-time function with half-duration of 5 s, which corresponds to the resolution period of the mesh used for this simulation.

Radial and transverse component seismograms as a function of backazimuth for this simulation are shown in Fig. 2, which demonstrates the expected behaviour of the transverse component waveform for azimuthal anisotropy (Vinnik *et al.* 1989; Chevrot 2000). While the radial component does not change much with azimuth, the transverse component is azimuthally dependent, and its shape takes the form of the time derivative of the radial component, multiplied by a scalar factor that depends on the angle between the initial polarization of the shear wave and the azimuth of the fast symmetry axis (as well as the strength of anisotropy). We observe the expected behaviour of no energy on the transverse component in the case where the initial polarization is parallel or perpendicular to the fast axis orientation (Fig. 2), and a maximum in transverse component energy when the initial polarization is 45° from the symmetry axis. Following eqs (7) and (A4) from Chevrot (2000), we measure the splitting intensity for each synthetic seismogram, which is defined as:

$$SI = -2\frac{T(t)R'(t)}{\|R'(t)\|^2}. \tag{3}$$

The splitting intensity measured as a function of backazimuth forms the splitting intensity vector which is shown in Fig. 3. Estimates of the splitting parameters ($\phi\ \delta t$) can be derived from fitting a $\sin(2\theta)$ curve to the splitting intensity vector shown in Fig. 3, using the relationship $SI \simeq -1/2\delta t \sin 2(\beta)$, where β corresponds to the angle between the initial polarization direction and the azimuth of the fast symmetry axis. Our estimates of the splitting parameters derived from Fig. 3 are $\phi = 45°$ and $\delta t = 0.228$ s, which agree well with the values for the same test in Chevrot (2000).

4 UPPER MANTLE ANISOTROPY SIMULATIONS AND COMPARISON WITH RAY THEORY

4.1 Background: upper mantle anisotropy and shear wave splitting

Seismic anisotropy in the upper mantle is generally interpreted in terms of the CPO of anisotropic upper mantle minerals, primarily olivine. The relationships between strain and the resulting CPO are complex and depend on many factors, potentially including stress, temperature, pressure, water content, deformation history and pre-existing fabric (e.g. Karato *et al.* 2008; Skemer & Hansen 2016). Despite these complications, however, a number of simplified relationships are often used to interpret *SK*(*K*)*S* splitting data, often with implicit assumptions made about the symmetry of the anisotropic medium. For example, upper mantle anisotropy is often modelled using a hexagonal approximation to the actual elastic tensor (e.g. Browaeys & Chevrot 2004; Becker *et al.* 2006), even though olivine itself is orthorhombic, and even though actual aggregates of mantle rocks may have even lower symmetry in practice. As discussed in the Introduction, the interpretation of *SK*(*K*)*S* data is usually done in the context of ray theory, with only a few exceptions. While a few studies have examined the finite-frequency sensitivity of *SK*(*K*)*S* splitting to upper mantle anisotropy (e.g. Favier & Chevrot 2003; Favier *et al.* 2004; Chevrot 2006; Long *et al.* 2008; Sieminski *et al.* 2008; Zhao & Chevrot 2011; Lin *et al.* 2014a), it is relatively uncommon to carry out global wavefield simulations to model the effects of upper mantle anisotropy on *SK*(*K*)*S* splitting. The purpose of the tests presented in this section is to establish the new

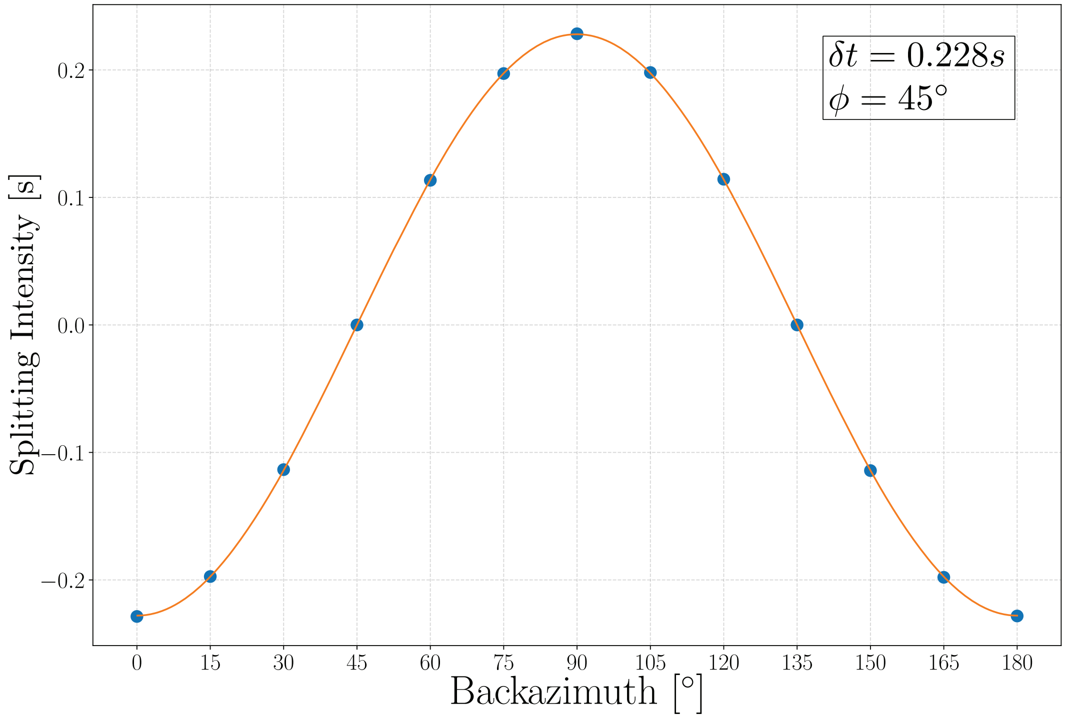

Figure 3. Result of the shear wave splitting intensity analysis performed on the synthetic seismograms of Fig. 2. The splitting intensity vector (blue dots) is computed following Chevrot (2000, eq. A4). The orange curve is the least square fit solution $s = \sin 2\theta(\phi - \phi_0)$, calculated over possible pairs of splitting intensity parameters ϕ and δt, that minimizes the misfit between the synthetic and the theoretical splitting intensity solution. The amplitude of the curve is 0.228 s and its phase is 45°. Compare this figure with (Chevrot 2000, fig. 3).

anisotropy module of AxiSEM3D as a viable tool for doing so, and to explore how anisotropy models of increasing complexity in terms of their symmetry (from hexagonal to orthorhombic) affect *SK*(*K*)*S* waveforms.

A second goal of these tests is to understand to what extent shear wave splitting measurements performed on synthetic seismograms derived from global wavefield simulations depart from the predictions of ray theory. Work by Lin *et al.* (2014a) established that full-wavefield effects on *SK*(*K*)*S* phases can cause significant deviations from ray theoretical predictions of shear wave splitting, even for relatively simple (laterally homogenous) upper mantle anisotropy models. We aim to extend our understanding of this phenomenon here, particularly as it relates to the interpretation of *SKS*−*SKKS* splitting discrepancies. Relatively large discrepancies between the splitting of *SKS* and *SKKS* phases for the same event-station pair are typically interpreted as evidence for a contribution to the splitting of one or both phases from anisotropy in the lower mantle (e.g. Niu & Perez 2004; Long 2009; Lynner & Long 2014; Grund & Ritter 2018; Reiss *et al.* 2019). However, Lin *et al.* (2014a) showed that wavefield effects that depart from the predictions of ray theory can cause small discrepancies in splitting intensity values (up to ∼0.3 s) between *SKS* and *SKKS* phases for models that only include upper mantle anisotropy. The work of Lin *et al.* (2014a) used computations of finite-frequency sensitivity kernels based on the formulation of Zhao & Chevrot (2011). Here we build on this work using a complementary method (global wavefield simulations as opposed to explicit sensitivity kernel computations).

In order to compare the splitting of synthetic *SK*(*K*)*S* waveforms to the predictions of ray theory (and eventually to real data), we measure both the splitting intensity introduced by Chevrot (2000), as described in Section 3.2, and the traditional splitting parameters (ϕ, δt) using the transverse component minimization method of Silver & Chan (1991). We use the implementation of the Silver & Chan (1991) method in **SplitRacer** (Reiss & Rümpker 2017), a MATLAB-based graphical user interface for teleseismic shear wave splitting analysis. We compare the splitting measurements made on synthetic waveforms with predictions from ray theory, derived from the Python tool **christoffel** (Jaeken & Cottenier 2016), which solves the Christoffel equation to predict the polarizations and velocities of the quasi-*S* phases for waves propagating over a range of directions.

4.2 Upper mantle case #1: horizontal transverse isotropy (HTI)

We now introduce a global wavefield simulation for a case that includes azimuthal anisotropy, in the form of a (single, laterally homogenous) anisotropic layer in the upper mantle with HTI symmetry. We do this simply by modifying the radially anisotropic upper mantle layer in PREM from a VTI symmetry to an HTI symmetry by rotating the symmetry axis by 90°. The symmetry axis thus lies in the horizontal plane for this simulation. The properties of the anisotropic layer are shown visually in Fig. 4, which shows representations of the anisotropic properties of various scenarios tested in this paper. The VTI elastic tensor of PREM is represented in Fig. 4, top row, while the rotated HTI tensor used in this test is shown in Fig. 4, second row. In order to avoid waveform complexity due to structural heterogeneity, we use a laterally homogeneous, 1-D earth model that corresponds to PREM except for in the depth range between 24 and 220 km, where we impose the HTI elastic tensor described above. We neglect attenuation and ellipticity in the simulation, even though this can be simulated with AxiSEM3D in general. We use a source and receiver configuration shown in the

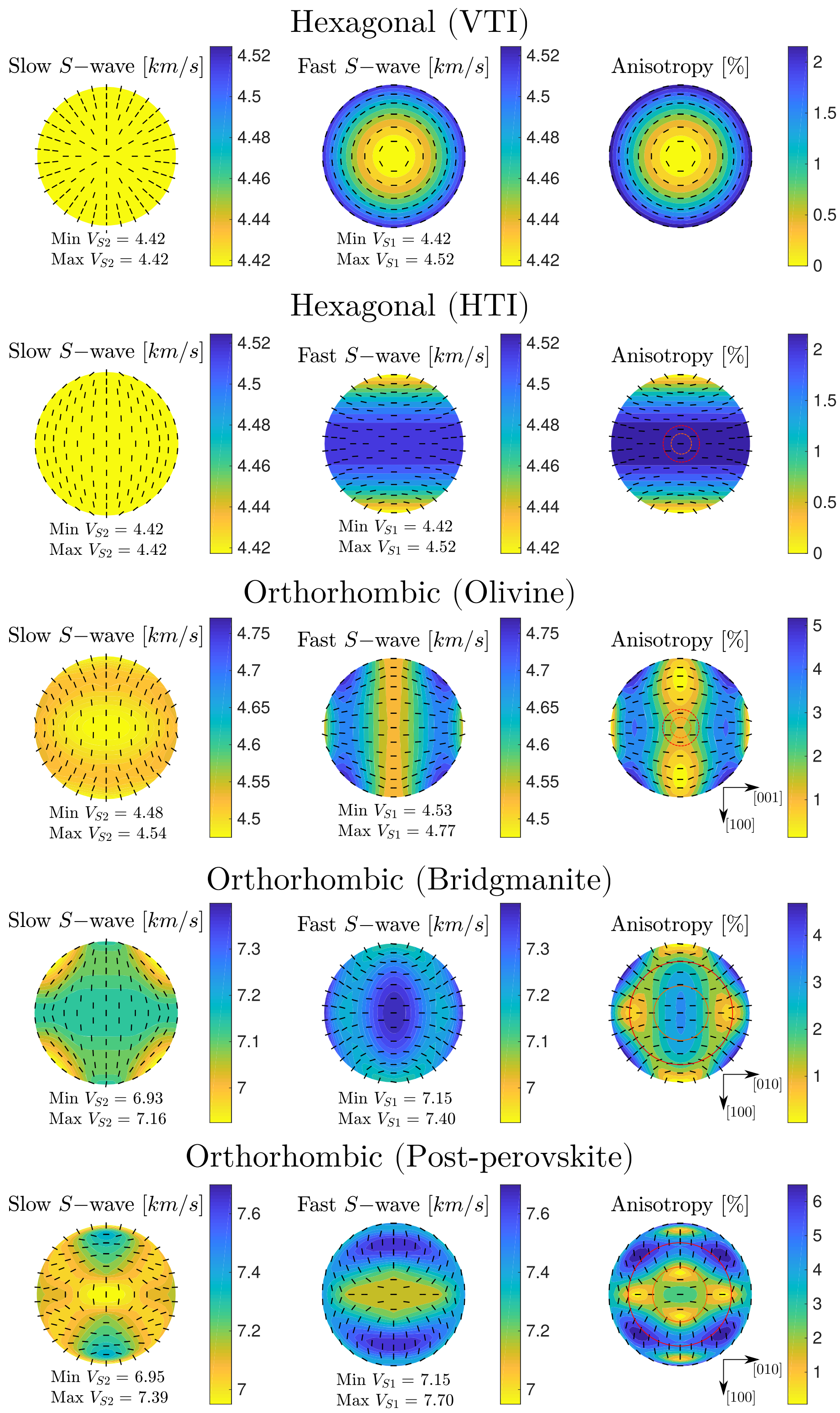

Figure 4. Polar view representation of different elasticity tensors belonging to different symmetry classes (from top to bottom hexagonal (VTI, HTI) and orthorhombic (olivine, bridgmanite, post-perovskite) used to describe the elastic and geometrical properties of the anisotropic regions tested in the different simulation settings. The magnitude of the slow and fast shear wave velocity and its polarization direction (black thick marks) are shown on the left-hand side and middle plots, respectively. A measure of the anisotropy is shown on the right plot along with the fast shear wave polarization direction (black thick marks). The VTI, HTI, and olivine tensors are used in examples where the anisotropy is localized in the upper mantle whereas the bridgmanite and post-perovskite are used in the D''. The orientation of the othorombic crystals are specified by the 2 orthogonal crystallographic axes that lie in the horizontal plane. The dashed concentric circles in the HTI and olivine tensors mark the region of the piercing points for the *SKS* (orange) and *SKKS* (red) phases in the upper mantle, while the solid circles indicate the region of the piercing points for the bridgmanite and post-perovskite crystals in the D'' layer.

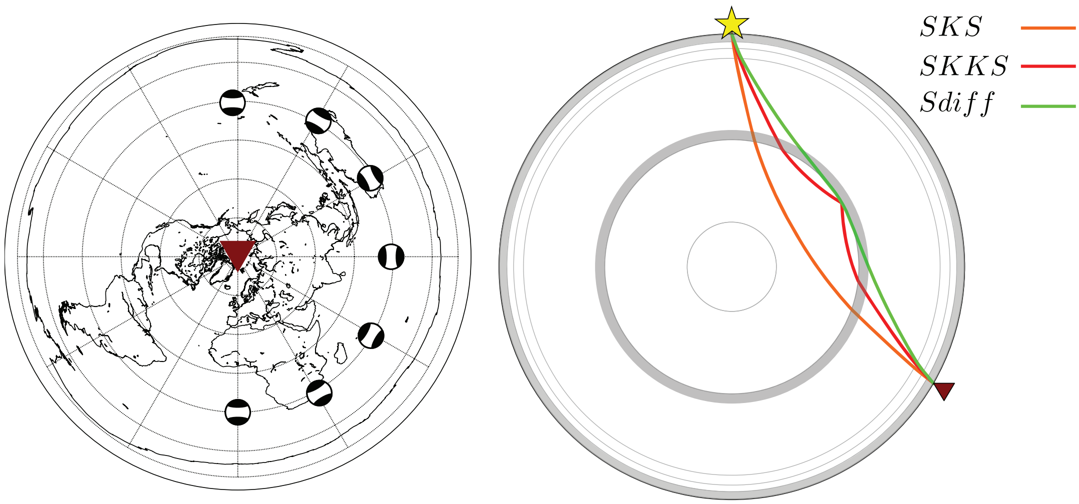

Figure 5. Left-hand panel: source–receiver distribution for global seismic wavefield simulations in anisotropic Earth-like models. The red triangle marks the centre of the array of receivers located at the North Pole at a distance of 120° from the seismic sources. The sources span a fan of 180° along the azimuthal direction with interspacing of 15°. Right-hand panel: diagram of ray-theoretical paths of seismic *S* phases commonly used in share wave splitting analysis. The paths for *SKS*, *SKKS* and S_{diff} are shown as reference for a source (star) and the receiver (red triangle) at 120° of epicentral distance. The shaded grey areas represent the two anisotropic regions between 24 and 220 km in the upper mantle and 250 km at the top of the core–mantle boundary in the D''. Paths are calculated using **TauP** (Crotwell *et al.* 1999) for the PREM velocity model (Dziewonski & Anderson 1981).

left-hand panel of Fig. 5, with the source located at the surface (to avoid depth phases resulting from reflections off the free surface). The receiver is located at the North Pole, while the sources are located at 15° azimuthal intervals at an epicentral distance of 120°, at which both *SKS* and *SKKS* phases should be visible (e.g. Long 2009). The moment tensor for each source is chosen to maximize the radiation of *S* wave energy in the direction of the receiver, as shown in Fig. 5. While our simulations reproduce the entire wavefield, we focus on the portions of the synthetic seismograms that show the *SKS*, *SKKS* and S_{diff} phases; the ray-theoretical paths of these phases are shown in the right-hand panel of Fig. 5. The synthetic seismograms for the radial and transverse components plotted against the backazimuthal direction of the incoming wavefield are shown in Fig. 6 in a time-window that includes *SKS*, *SKKS* and S_{diff} phases. We also show synthetic waveforms as a function of backazimuth for epicentral distances of 100° and 110° in the Supporting Information (Figs S1–S2).

The splitting analysis results of this simulation are shown in Fig. 7, which shows the measured splitting intensity as a function of backazimuth from the synthetic seismograms for *SKS* and *SKKS* phases, along with the predictions from ray theory. The ray theoretical predictions were obtained by solving the Christoffel equation for an elasticity tensor that was averaged over the depth range of the anisotropic layer, with the *SKS* and *SKKS* propagation directions derived from **TauP** (Crotwell *et al.* 1999) for the PREM model. As expected, the measured splitting intensity values exhibit a variation with backazimuth that is close, but not identical, to that predicted by ray theory (solid orange and dashed red curves in Fig. 7). The full wavefield solution yields splitting intensity values that are systematically smaller, by up to ∼0.25 s, than the ray theoretical predicted values. Similar to Lin *et al.* (2014b), we also find modest differences in *SKS* and *SKKS* splitting intensity, of up to ∼0.2 s, at certain azimuths, with the difference being largest at a backazimuth that is 30° from the fast direction. We retrieve the best-fitting splitting parameters (ϕ, δt) for *SKS* and *SKKS*, respectively, by fitting a $sin(2\theta)$ curve to the splitting intensity measurements in Fig. 7, and obtain values of $\phi = 90°$ and $\delta t = 0.780s$ for *SKS* and $\phi = 90°$ and $\delta t = 0.862s$ for *SKKS*. These values generally compare well to the ray theoretical values of $\delta t = 1.036s$ for *SKS* and $\delta t = 1.038s$ for *SKKS*, although again, ray theory overpredicts the amplitude of the splitting compared to the wavefield simulations. Finally, we compare the splitting parameters obtained from the splitting intensity curve to those obtained by the transverse component minimization method at two representative backazimuths, shown in Fig. 8. As with the splitting intensity measurements, there are modest differences in measured splitting parameters between *SKS* and *SKKS* phases at the same backazimuth, although in this case these differences are not significant considering the error estimates (Fig. 8).

4.3 Upper mantle case #2: orthorhombic symmetry

We now explore a case in which the upper mantle anisotropic layer has a lower symmetry class. Because CPO of olivine is generally understood to be the main cause of upper mantle anisotropy, and because single-crystal olivine has an orthorhombic symmetry, it is reasonable to test an orthorhombic model. Single-crystal olivine has a strong anisotropy, up to ∼25 per cent for *P* waves and ∼22 per cent for *S* waves, according to laboratory measurements (Babuska & Cara 1991; Isaak 1992; Abramson *et al.* 1997; Mao *et al.* 2015). The bulk anisotropy in deformed olivine aggregates, however, is significantly lower than the single-crystal anisotropy (e.g. Ben Ismaïl & Mainprice 1998; Karato *et al.* 2008). We constructed a model for upper mantle anisotropy by taking an averaging approach that preserves the symmetry class of the orthorhombic single crystal but decreases its anisotropy strength. We used the **MSAT** code (Walker & Wookey 2012) to calculate a linear mixture consisting of 30 per cent San Carlos single-crystal olivine at upper mantle conditions, as described by Abramson *et al.* (1997), and 70 per cent isotropic PREM. The resulting elasticity tensor (Fig. 4, third row) has a similar symmetry of a single crystal of olivine (we choose an orientation such that the [100] and [001] axes are in the horizontal direction, and the [010] axis is oriented vertically), but the

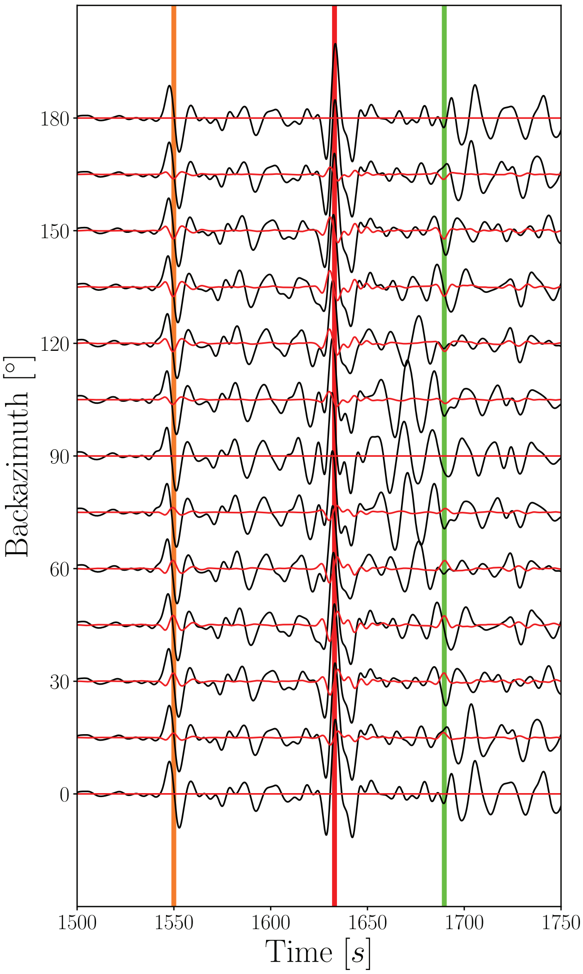

Figure 6. Synthetic seismograms computed for the PREM model with a HTI layer localized between 24 and 220 km plotted against the backazimuth of the incoming seismic energy. The epicentral distance is 120°. The radial component is shown in black and the transverse is shown in red. Predicted arrival time for *SKS*, *SKKS* and S_{diff} are shown as the vertical orange, red and green bars, respectively.

anisotropy is substantially weaker (∼5 per cent maximum). As in the HTI upper mantle simulation, the anisotropic layer is confined between 24 and 220 km depth.

We show the results of our wavefield simulation in Fig. 9, which is similar to Fig. 7 but for the orthorhombic symmetry case. Synthetic seismograms across a range of backazimuths at epicentral distances of 100°, 110° and 120° for this simulation are shown in the Supporting Information (Figs S3–S5). Because of the departure from hexagonal symmetry, the ray theoretical predictions (solid orange and dashed red lines in Fig. 9) are no longer perfect sin (2θ) curves, and in this case ray theory predicts some discrepancies between *SKS* and *SKKS* phases at certain azimuths. The measured splitting intensity values from the synthetic seismograms show some departures from the ray theoretical predictions, as in the HTI simulation, but for the orthorhombic case the departures are more pronounced (compare Fig. 9 with Fig. 7). As with the HTI case, there are a few azimuths for which we find discrepancies in *SKS*−*SKKS* splitting intensities; somewhat surprisingly, this discrepancy is quite large (difference in splitting intensity of ∼0.4 s) at backazimuths that lie 45° away from the fast splitting direction. An examination of the transverse component minimization measurements at selected backazimuths (Fig. 10) shows that the *SKKS* splitting measurement at a backazimuth of 45° is poorly constrained due to a stronger interference of a not well identifiable phase on the radial component that leads to the contamination of the splitting measurements.

5 LOWERMOST MANTLE ANISOTROPY SIMULATIONS AND COMPARISON WITH RAY THEORY

5.1 Background: lowermost mantle anisotropy and shear wave splitting

We now turn our attention to seismic anisotropy in the lowermost mantle, which has been the subject of a great deal of recent observational work (e.g. Wookey *et al.* 2005a; Long 2009; Nowacki *et al.* 2010; Cottaar & Romanowicz 2013; Lynner & Long 2014; Ford *et al.* 2015; Creasy *et al.* 2017; Grund & Ritter 2018; Reiss *et al.* 2019), but which is substantially more challenging to observe than upper mantle anisotropy. As summarized in Nowacki *et al.* (2011) and Creasy *et al.* (2019), there are a variety of possible mechanisms that may contribute to anisotropy in the D'' layer, including CPO of bridgmanite or post-perovskite (depending on which mineral dominates, which may in turn depend on the temperature in a given region of D'' (Houser 2007)), CPO of ferropericlase, or shape-preferred orientation (SPO) of elastically distinct material such as partial melt. We do not test all of these possible mechanisms in this paper; instead, we test models of aligned post-perovskite and aligned bridgmanite, one of which is expected to be the most volumetrically important phase in any given region of D''. Testing of other models for D'' anisotropy will be left to future work.

There are a variety of strategies for measuring D'' anisotropy using body waves, only some of which rely on *SK*(*K*)*S* phases. One common approach is to measure the differential splitting of *S*−*ScS* phases [introduced by Wookey *et al.* (2005a); see also Wookey & Kendall (2008); Ford *et al.* (2015); Rao *et al.* (2017)] or to examine the waveform behaviour of phases such as S_{diff} (e.g. Cottaar & Romanowicz 2013). The identification of significant discrepancies between the splitting of *SKS* and *SKKS* phases for the same event–station pair, first documented by James & Assumpção (1996), have been attributed to anisotropy at the base of the mantle beginning with Niu & Perez (2004) and Restivo & Helffrich (2006). The measurement of *SKS*−*SKKS* splitting discrepancies to study D'' anisotropy is becoming more common (e.g. Long 2009; He & Long 2011; Roy *et al.* 2014; Lynner & Long 2014, 2015; Grund & Ritter 2018), although there is some debate about the extent to which *SKS*−*SKKS* splitting discrepancies require a contribution to the lowermost mantle. Some studies (Monteiller & Chevrot 2011; Lin *et al.* 2014a) have argued that *SKS*−*SKKS* splitting discrepancies can be explained solely in terms of upper mantle anisotropy. Recently, some studies of *SKS*−*SKKS* splitting discrepancies have come to rely on the measurement of splitting intensity, rather than the traditional splitting parameter estimation methods, on the grounds that the splitting intensity is a more robust and stable measurement (Deng *et al.* 2017; Reiss *et al.* 2019). Despite ample observational evidence that *SK*(*K*)*S* phases can indeed be affected by anisotropy in the lowermost mantle, there is still no consensus in the literature about how strong the finite-frequency sensitivity of these phases is to anisotropy in D'' (Sieminski *et al.* 2008; Zhao & Chevrot 2011). Furthermore, there are disagreements in the literature about to what extent documented *SKS*−*SKKS* splitting discrepancies reflect a contribution to splitting from lowermost mantle anisotropy to one or

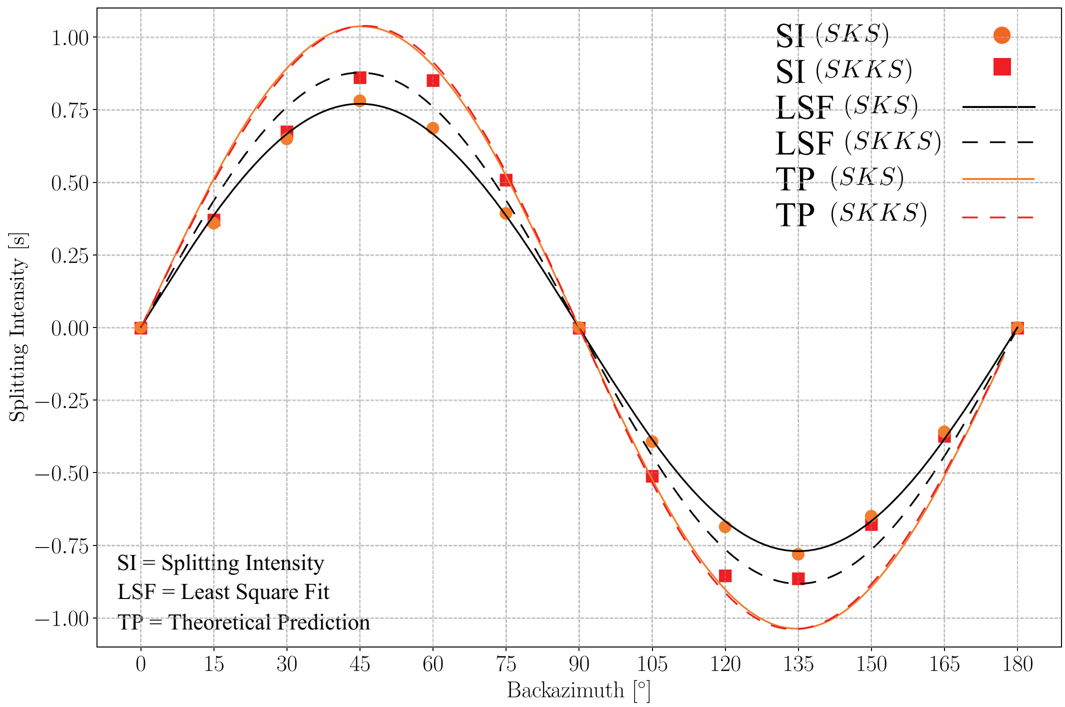

Figure 7. Shear wave splitting intensity analysis performed on the synthetic seismograms evaluated for the PREM model with HTI (see Fig. 4, second row) localized between 24 and 220 km depth. Values of the splitting intensity vector calculated for *SKS* are shown as orange circles while for *SKKS* are shown as red squares. The black solid and dashed curves represent the two least square fit solutions for *SKS* and *SKKS*, respectively. The orange solid and dashed red lines are the ray-theoretical predicted splitting intensity vectors for *SKS* and *SKKS* respectively, evaluated by solving the Christoffel equation for an elasticity tensor that was averaged over the depth range of a ∼200-km-thick anisotropic layer in the upper mantle.

both phases (e.g. Niu & Perez 2004; Restivo & Helffrich 2006; Long 2009), or whether such discrepancies can mainly be attributed to upper mantle anisotropy (e.g. Monteiller & Chevrot 2011; Lin *et al.* 2014a). There is, therefore, a need for global wavefield simulations that include lower mantle anisotropy.

Another argument for the study of full-wave effects of D'' anisotropy on *SK*(*K*)*S* phases comes from recent work that has sought to carry out forward modelling of D'' anisotropy, relying on results from mineral physics (e.g. Walker *et al.* 2011; Cottaar *et al.* 2014; Ford *et al.* 2015; Ford & Long 2015; Creasy *et al.* 2017, 2019; Walker *et al.* 2018; Tommasi *et al.* 2018). These types of modelling studies tend to rely exclusively on ray theory, with very few exceptions (e.g. Nowacki & Wookey (2016), who looked at full-wave effects for complex anisotropic models but who only considered *ScS* phases). Given the popularity of these types of modelling approaches, it is crucial to understand how well the ray theoretical approximation captures the true behaviour of *SK*(*K*)*S* waves.

5.2 Lowermost mantle case #1: bridgmanite crystallographic preferred orientation

We first consider a case that invokes a laterally homogeneous, 250-km-thick D'' layer at the base of the mantle, with elasticity that is designed to capture the first-order characteristics of aligned bridgmanite. Because the dominant slip systems at lowermost mantle conditions remain uncertain, we follow the strategy of recent modelling studies (e.g. Ford *et al.* 2015; Creasy *et al.* 2017) and consider tensors based on single-crystal elasticity. We chose an orientation such that the [100] and [010] axes of bridgmanite are oriented in the horizontal direction, while the [001] axis is vertical. We create an elastic tensor via a linear mixture of 30 per cent single crystal anisotropy of post-perovskite, using the elastic constants from Wookey *et al.* (2005b), with 70 per cent of isotropic PREM at D'' depths. This mixing ratio yields an elastic tensor with an orthorhombic symmetry and with a maximum anisotropy of 6 per cent, as shown in Fig. 4, fourth row. As with the upper mantle cases, we propagate the seismic wavefield through this model using the source and receiver geometries shown in Fig. 5, and measure the splitting intensity, as well as the traditional shear wave splitting parameters, as a function of backazimuth. Also as with the upper mantle cases, we compare the synthetic splitting measurements with predictions from ray theory. In contrast to the upper mantle case, in the lowermost mantle the *SKS* and *SKKS* phases under study have significantly different ray propagation paths. Using **TauP** (Crotwell *et al.* 1999), we calculated nominal propagation angles (from the horizontal) through the D'' region of 67° for *SKS* and 42° for *SKKS*.

Results from our bridgmanite simulation are shown in Figs 11 and 12. Synthetic seismograms across a range of backazimuths at epicentral distances of 100°, 110° and 120° for this simulation are shown in the Supporting Information (Figs S6–S8). Because the ray paths of *SKS* and *SKKS* phases depart so significantly from the vertical, we no longer expect a simple $\sin 2(\theta)$ variability in the splitting intensity curve, and this is borne out by the measurements on synthetic seismograms. For this reason, we do not fit a $\sin 2(\theta)$ curve to our measurements, as we did for the upper mantle cases. We do predict the ray theoretical splitting intensity curves, as shown on Fig. 11; these are based on the predicted apparent splitting parameters at each azimuth, visualized in Fig. 4, fourth row. As with the upper mantle cases, particularly the HTI simulation, we find that the full-wavefield simulations predict splitting intensity behaviour that is generally similar to the ray theoretical predictions, but not identical to it. We see deviations of up

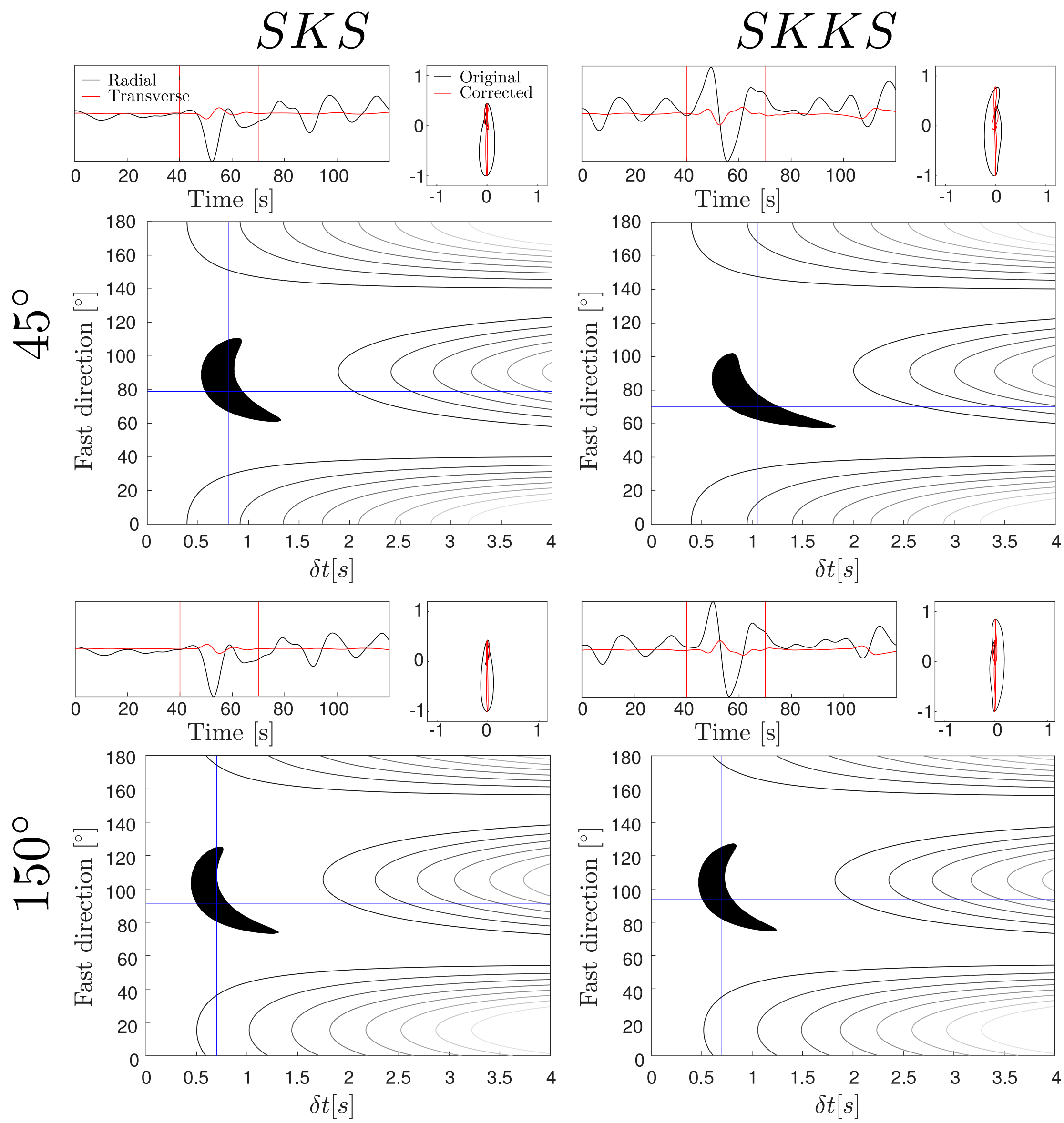

Figure 8. Shear wave splitting analysis performed using the transverse component minimization method (Silver & Chan 1991) on the *SKS* (left-hand panel) and *SKKS* (right-hand panel) phases for 2 representative backazimuthal propagation directions of the incoming seismic energy (45° and 150°). The synthetic seismograms are evaluated for a PREM model with a HTI layer localized between 24 and 220 km as in Fig. 7. Each panel is composed by 3 plots: On the top left a 120 s long time-window with the radial (black) and transverse (red) component synthetic seismograms. The vertical red bars mark the phases on which the analysis is performed. On the top right corner we show the original and the corrected particle motion. In the bottom plot we show the energy map with the calculated splitting parameters and the 95 per cent confidence interval as the shaded black area. For this configuration *SKS* and *SKKS* yield a comparable results for both fast direction axis and delay-time.

to ∼0.2 s in splitting intensity values between the ray theoretical predictions and the synthetic seismogram measurements at certain azimuths, again similar to what is observed for the upper mantle cases. Importantly, the bridgmanite model predicts spitting intensities of up to ∼0.8 s for *SKS* and *SKKS* phases, nearly as large as the maximum values predicted from ray theory, indicating that these phases have significant sensitivity to anisotropy at the base of the mantle. Notably, both the synthetic seismogram measurements and the ray theoretical predictions indicate that at certain azimuths, significant discrepancies between *SKS* and *SKKS* splitting intensities are expected, even though the underlying model is laterally homogeneous.

5.3 Lowermost mantle case #2: post-perovskite crystallographic preferred orientation

Finally, we test a model that invokes aligned post-perovskite as the cause for D'' anisotropy. The phase transition from bridgmanite to post-perovskite, which was discovered experimentally by Murakami *et al.* (2004), is thought to be the cause of the D'' discontinuity, and is expected to dominate in relatively cold regions of the lowermost mantle (e.g. Hernlund *et al.* 2005), and perhaps throughout (e.g. Koelemeijer *et al.* 2018). Post-perovskite is generally favoured as the most likely mechanism for D'' anisotropy by many authors (e.g. Nowacki *et al.* 2010; Walker *et al.* 2011; Cottaar *et al.* 2014; Ford *et al.* 2015). Similar to our test for bridgmanite, we create an

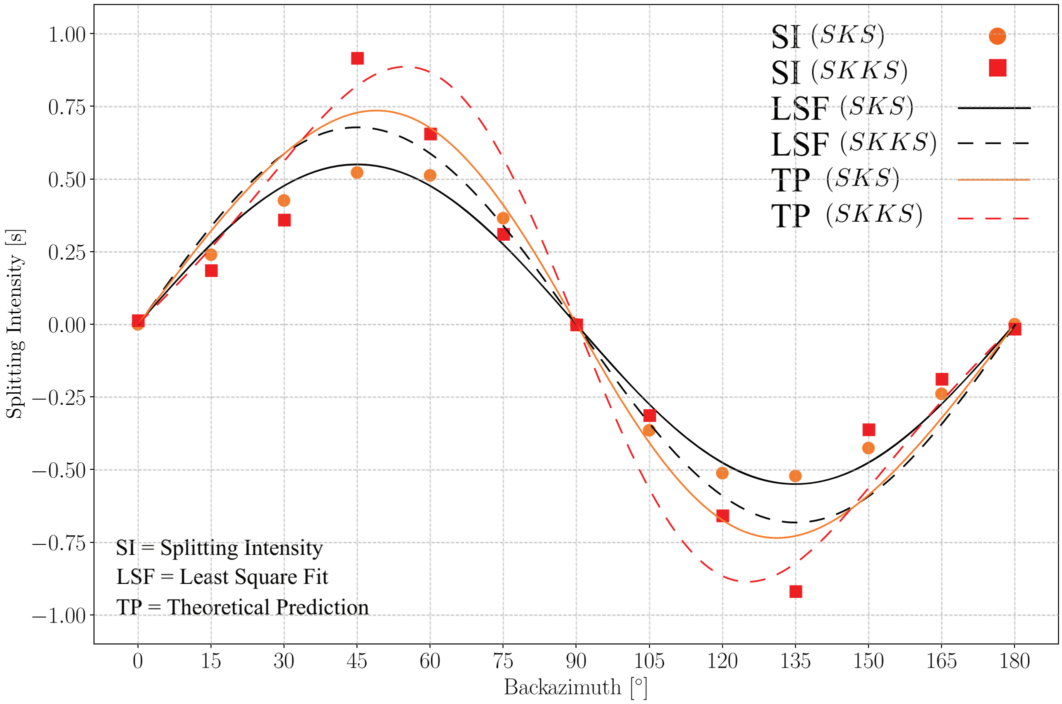

Figure 9. Same as Fig. 7 but with the anisotropic region in upper mantle between 24 and 220 km described with an orthorhombic elasticity tensor (see Fig. 4, third row). The elastic properties of the tensor are the result of a linear mixture of 30 per cent of San Carlos single crystal olivine from Abramson *et al.* (1997) and 70 per cent PREM. The least square fit solutions and the theoretical predicted splitting intensity vectors are also plotted with the same colour code used in Fig. 7.

elastic tensor that is a linear mixture of 30 per cent single crystal anisotropy, using elastic constants for post-perovskite from Wookey *et al.* (2005b), and 70 per cent isotropic PREM. In this scenario, we assume that the [100] and [010] axes are oriented in the horizontal directions, while the [001] axis is vertical. Predicted ray theoretical splitting patterns for this tensor are shown in Fig. 4, bottom row.

Results from our post-perovskite wavefield simulation, along with ray theoretical predictions for this scenario at the relevant azimuths, are shown in Figs 13 and 14 shows representative transverse component minimization splitting measurements at two azimuths. Synthetic seismograms across a range of backazimuths at epicentral distances of 100°, 110° and 120° for this simulation are shown in the Supporting Information (Figs S9–S11). Interestingly, for this orientation of the post-perovskite elasticity tensor, *SKS* phases are split only very weakly, with maximum splitting intensities of ∼0.2 s. This is consistent with the ray theoretical prediction for *SKS* splitting behaviour (Fig. 13; see also Fig. 4, bottom row). The behaviour of *SKKS* phases provides a striking contrast; for the propagation angles relevant for *SKKS*, this elastic tensor scenario predicts strong splitting, with maximum splitting intensities of ∼2.5 s. The azimuthal variation in the *SKKS* splitting intensities measured from the synthetic seismograms is to first order captured by the ray theoretical prediction (Fig. 13), although the synthetic splitting intensities are generally lower (sometimes by as much as ∼1.0 s) than the values predicted by ray theory. For the traditional splitting measurements (Fig. 14), the splitting of *SKS* phases is so slight that there is not enough transverse component energy to obtain a stable measurement; as expected, these measurements do not yield meaningful splitting parameter estimates. For the *SKKS* phases, in contrast, the transverse component minimization method yields robust measurements with strong splitting, consistent with the splitting intensity measurements (Fig. 13) and as predicted by ray theory.

6 CROSS-VERIFICATION AGAINST AN INDEPENDENT 3-D SPECTRAL ELEMENT SOLVER

Here we present a verification of our implementation of full anisotropy in AxiSEM3D by a benchmark solution against SPECFEM3D_GLOBE (Komatitsch & Tromp 2002a,b). It is important to point out that the following benchmark test should be regarded as a cross-verification rather than a validation *per se*, as SPECFEM3D_GLOBE has not yet been benchmarked for global wavefield propagation in arbitrary anisotropic earth models. We use the global-scale 3-D anisotropic model of Montagner (2002), based on surface wave tomography, which includes both radial and azimuthal anisotropy. This model spans between the Moho (24 km) and the 670 km discontinuity and has a 5° horizontal resolution. Its elasticity tensor is determined by 13 independent parameters, numerically implemented as a fully anisotropic tensor with 21 independent parameters in both SPECFEM3D_GLOBE and AxiSEM3D. The benchmark problem, shown in Fig. 15, is based upon simulating an earthquake source located in Virginia at a depth of 12 km, corresponding to the 2011 $M_w = 5.8$ earthquake in Mineral, VA. The source time function is an error function with half-duration of 10 s. The synthetic seismograms are computed at 129 stations of the Global Seismographic Network (GSN) distributed across the Earth's surface (Fig. 15). Attenuation is turned off and the record length of the seismogram is 3600 s. A nearly perfect agreement has been achieved between SPECFEM3D_GLOBE and AxiSEM3D in this simulation.

In Fig. 16, we show the vertical components of a set of synthetic seismograms for stations (blue triangles in Fig. 15) in the ∼90−130° range of epicentral distance. In this set of synthetic traces, which show a range of body wave arrivals as well as surface waves, the

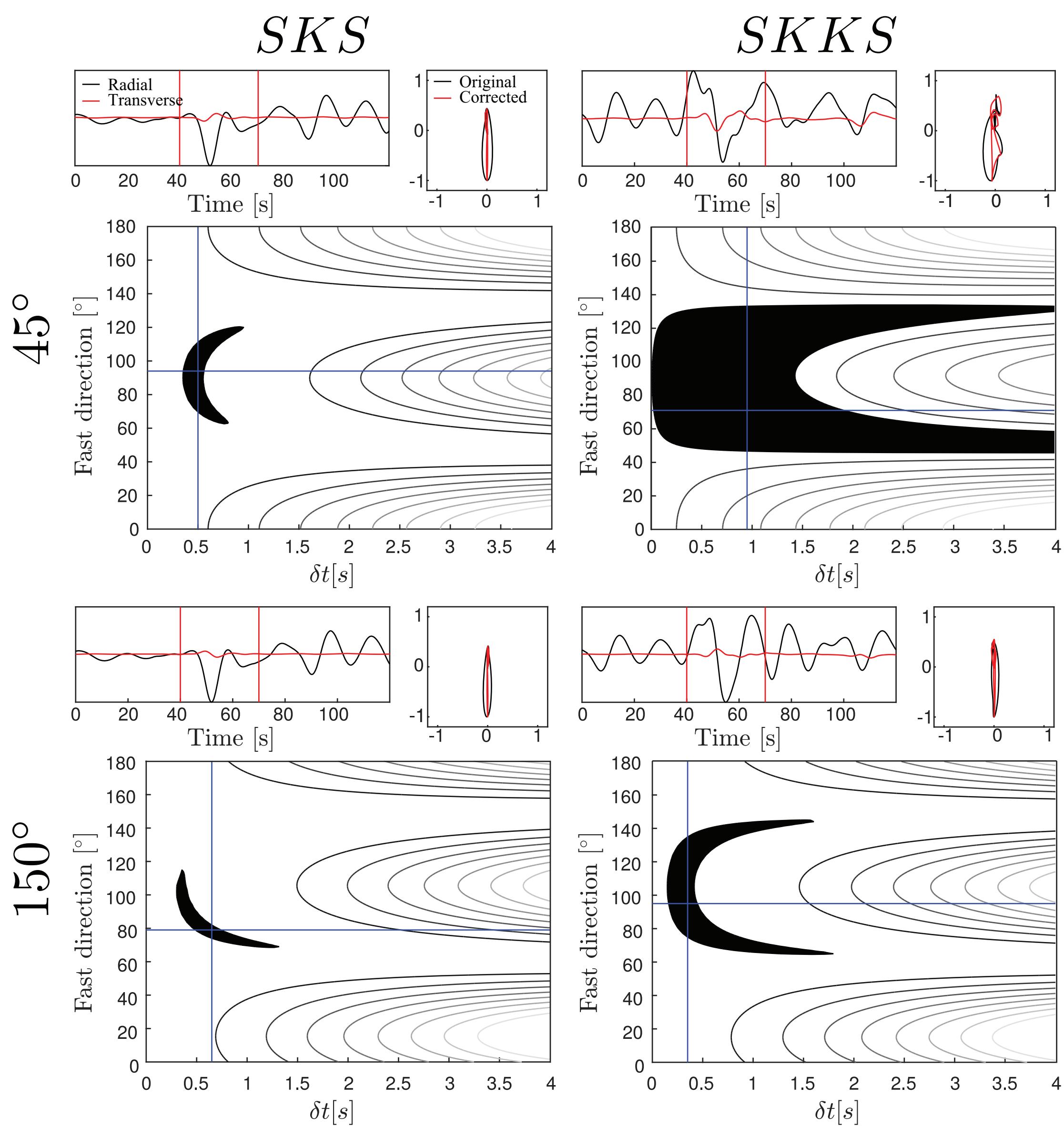

Figure 10. Same as Fig. 8 but with the anisotropic region in the upper mantle between 24 and 220 km being descried with an elasticity tensor of orthorhombic class which mimics the elastic properties of a horizontally strained olivine (see Fig. 4, third row). The splitting parameter estimates are less well constrained, with larger formal errors, than for the hexagonal upper mantle simulation shown in Fig. 8.

SPECFEM3D_GLOBE and AxiSEM3D traces are virtually indistinguishable. For reference, we also show corresponding synthetic seismograms computed for the radially anisotropic PREM, demonstrating the effect of the anisotropic structure in the Montagner (2002) model on the waveforms. Because the Montagner (2002) model only includes structure in the upper mantle, the major differences with PREM manifest in the upper mantle phases (*SS*, *SSS*) and the surface waves.

In Fig. 17, we show the same set of synthetics, but we zoom in on the time window shown in Fig. 16, to highlight the *SKS* and *SKKS* arrivals. We show both radial (top panel) and transverse (bottom panel) component records; the latter shows the effect of azimuthal anisotropy in the Montagner (2002) model. The same version of this figure for the vertical component is shown in the Supplementary Information (Fig. S12). For the transverse component traces in Fig. 17 (bottom panel), the PREM model predicts no energy associated with the *SKS* or *SKKS* time window; because PREM does not include azimuthal anisotropy, no splitting of *SK*(*K*)*S* phases is predicted. The SPECFEM3D_GLOBE and AxiSEM3D synthetics, in contrast, show significant transverse component *SK*(*K*)*S* energy at several of the selected stations. Again, the SPECFEM3D_GLOBE and AxiSEM3D traces are virtually indistinguishable in the time windows associated with *SK*(*K*)*S* arrival. We also report in the Supporting Information the full record section for the radial, transverse and vertical component of the all the stations localized in the $\sim 90-130°$ range of epicentral distance (Figs S13–S15). We do note some extremely small differences on the transverse components between the SPECFEM3D_GLOBE and AxiSEM3D traces in *PS* and *PPS* phases at some stations (e.g. II.MSVF). These differences are not visible on the corresponding

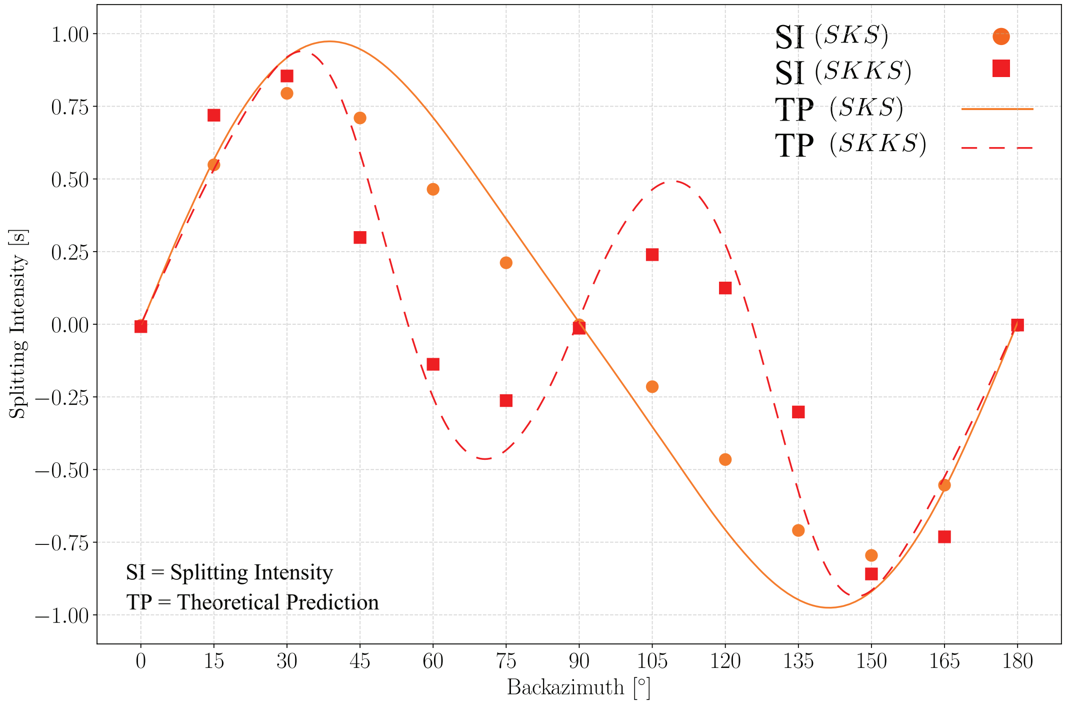

Figure 11. Splitting intensity analysis performed on synthetic seismograms evaluated for the PREM model with anisotropy localized at the base of the lower mantle in a 250-km-thick D'' layer. The elasticity tensor is composed of a linear mixture of 30 per cent bridgmanite from Wookey *et al.* (2005b) and 70 per cent isotropic PREM (see Fig. 4, fourth row). The splitting intensities for *SKS* (orange circles) and *SKKS* (red squares) are similar for some specific backazimuth propagation (0–30° and 150° and 180°) but show discrepancies between 45° and 135°.

radial components. These small differences are due to the fact that in general, phases with small amplitudes are more vulnerable to numerical errors (such as floating point errors and discretization errors). Because the two different methods have entirely different discretization schemes, some small differences for low-amplitude phases are expected.

Compared to a fully discretized 3-D method such as SPECFEM3D_GLOBE, AxiSEM3D has only one more parameter: the Fourier expansion order of the solution n_u (Leng *et al.* 2016, 2019). This parameter controls both the accuracy and the computational cost of AxiSEM3D. For a spherically symmetric earth model such as PREM, we have $n_u = 2$ everywhere in the 2-D computational domain of AxiSEM3D; in this case, AxiSEM3D degenerates to a pure axisymmetric spectral element method (Nissen-Meyer *et al.* 2014). For a 3-D model, the AxiSEM3D solution converges to the real 3-D solution as n_u increases, and its value for solution convergence is always much smaller (usually by orders of magnitude) than a fully discretized one for global wave propagation in a realistic 3-D earth models (Leng *et al.* 2016). It is most efficient to vary n_u with depth and epicentral distance to maximize the performance of AxiSEM3D. Convergence tests are common practice in AxiSEM3D and are thoroughly explained in Leng *et al.* (2016, 2019). We refer the reader to (e.g. Leng *et al.* 2016, fig. 11) and to Fig. S16 in the Supporting Information for a visual illustration of the convergence behaviour. In order to achieve the agreement demonstrated in Fig. 16 with SPECFEM3D_GLOBE, we have used $n_u = 400$ in the uppermost 200 km and $n_u = 100$ elsewhere. We enlarge n_u near the surface to have better accuracy for surface wave propagation. Such n_u field leads to highly accurate waveforms for all the phases at all the stations in Fig. 15. In terms of computer performance, with this n_u field, we have obtained a speedup of ∼6 compared to SPECFEM3D_GLOBE. This speedup can be further increased in case neither surface waves nor multiple bouncing body waves (*SSS*, *SSSS*) are of interest. The technique of wavefield scanning (Leng *et al.* 2019) can be used to fully optimize n_u for better performance.

A key aspect of AxiSEM3D is its ability to correctly account for off great-circle scattering at minimal computational cost, via the Fourier expansion approach. This capability has been extensively discussed in previous papers (Leng *et al.* 2016, 2019), which include previous benchmark tests of the AxiSEM3D code against SPECFEM3D_GLOBE. Because the Montagner (2002) model involves strong upper mantle heterogeneity, and thus causes strong scattering from out-of-plane structure, the benchmark test presented here provides a clear demonstration of the ability of AxiSEM3D to capture the complex properties of scattering by anisotropic heterogeneities in 3-D.

7 DISCUSSION

7.1 A tool for efficient global wavefield modelling in arbitrary anisotropic media

The series of benchmark tests and global wavefield simulations presented in this paper establishes the AxiSEM3D code as an efficient tool for modelling of the global wavefield in earth models that include anisotropy with arbitrary symmetry. In contrast to other 3-D wavefield simulation methods, AxiSEM3D simulations can be run at periods that are relevant for studies of *SK*(*K*)*S* splitting (down to ∼5−10 s period) at relatively modest computational cost due to the sparse sampling of smoothness in the azimuthal wavefield. For

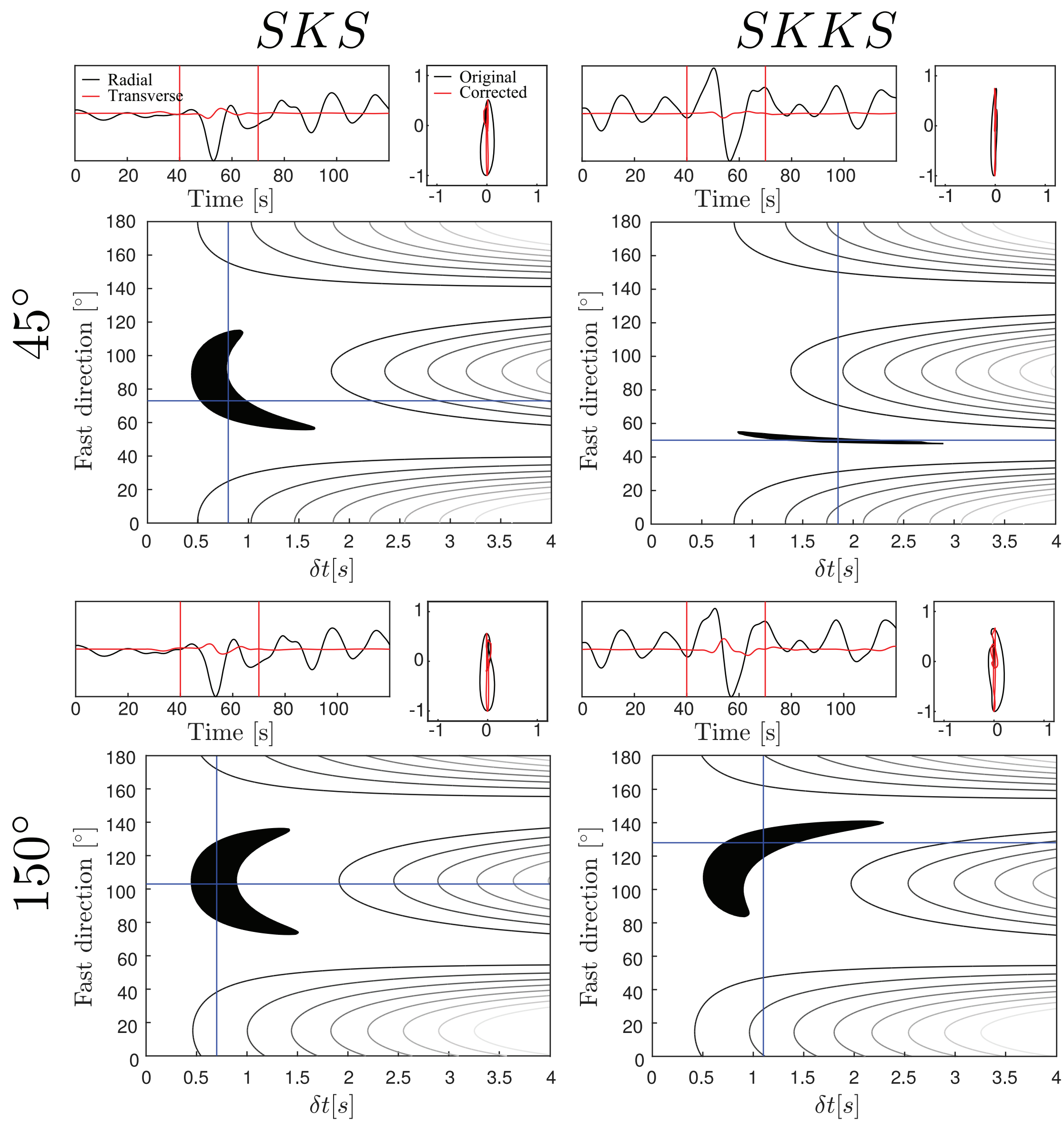

Figure 12. Same analysis presented in Fig. 8 but with orthorhombic style anisotropy in the form of a bridgmanite crystal localized in a 250-km-thick D'' layer. As for the splitting intensity analysis, we can see a similar result for *SKS* and *SKKS* in the case of seismic energy coming from 150° backazimuthal direction and discrepant results for 45°. We caution, however, that for the 45° backazimuth the *SKKS* splitting measurement is not well constrained.

example, the computational requirements for the global simulations presented in this paper involved about 3 hr and 30 min (wall-clock time) on 40 cores to produce 2000-s-long synthetic seismograms that can resolve seismic periods of 5 s.

The benchmarking tests presented in Section 3 serve to validate the implementation of arbitrary anisotropy in AxiSEM3D. In the first case, we ran a global simulation for the PREM model, including radial anisotropy, in two ways: one in which the model was specified in terms of vertical and horizontal wave velocities in the anisotropic layer, and one in which the same model was specified in terms of the equivalent full elastic tensor C_{ijkl}. The two solutions were found to be numerically identical, as expected. In the second test, we replicated a synthetic test presented in Chevrot (2000) that included azimuthal anisotropy. This test successfully demonstrated the azimuthal dependence of transverse component waveforms, with the expected waveform shape, and reproduced the expected splitting parameters (as measured via the splitting intensity) found by Chevrot (2000) for this model case. The simulations for upper and lowermost mantle anisotropy presented in Sections 4.1 and 5 demonstrate the feasibility of interrogating wavefield behaviour due to anisotropy effects in the context of global models using AxiSEM3D, and the cross-validation tests with SPECFEM3D_GLOBE presented in Section 6 yield a remarkable agreement between the two solutions, with a significant computational advantage obtained by AxiSEM3D.

7.2 Full wave sensitivity of *SK*(*K*)*S* phases to upper and lowermost mantle anisotropy

The upper mantle anisotropy models presented here build on previous work on the finite-frequency sensitivity of *SK*(*K*)*S* phases to azimuthal anisotropy in the upper mantle by a number of authors (e.g. Favier & Chevrot 2003; Favier *et al.* 2004; Lin *et al.*

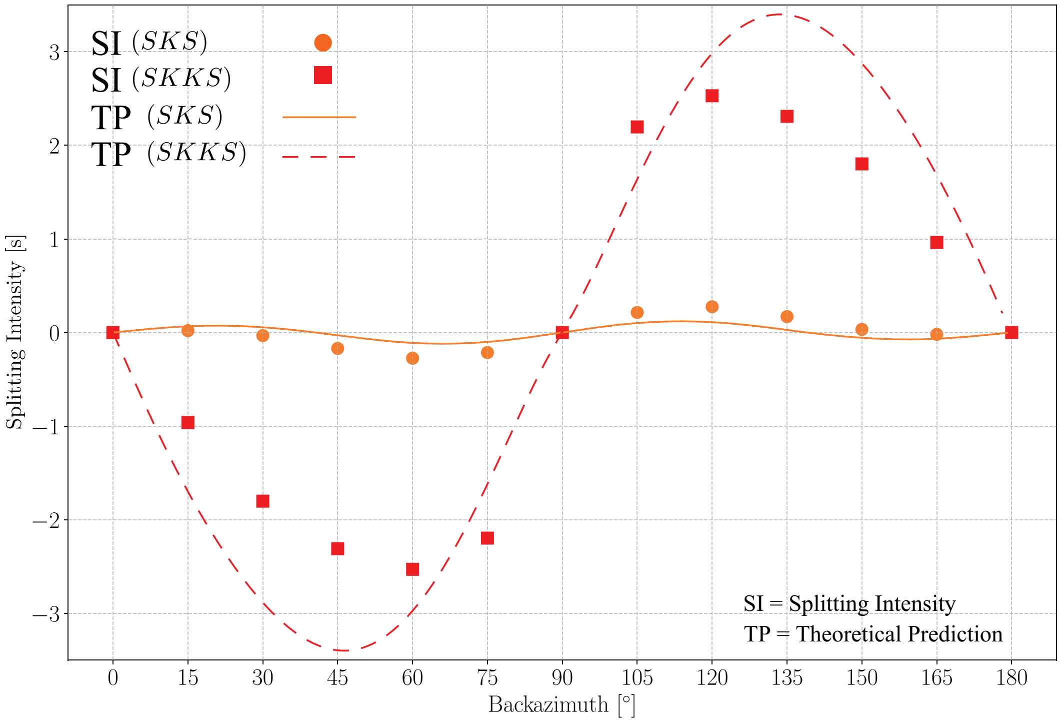

Figure 13. Same as Fig. 11 but with an elasticity tensor describing a post-perovskite mineralogy (see Fig. 4, bottom row). Strong discrepancies between *SKS* and *SKKS* are observed in this case for all the backazimuthal propagation directions with a very strong splitting observed for the *SKKS* and no splitting (null measurement) observed for the *SKS*.

2014a; Mondal & Long 2019) using a different set of tools (global wavefield simulations rather than sensitivity kernel computations). Similar to previous workers, we have found here that for laterally homogeneous models, ray theoretical approximations to the effects of upper mantle anisotropy on *SK*(*K*)*S* splitting are generally accurate to first order. However, similar to Lin *et al.* (2014a), we also found that at certain azimuths and epicentral distance ranges, full waveform effects can produce modest deviations from the predictions of ray theory. Unlike Lin *et al.* (2014a), we examined models in our study with orthorhombic symmetry (in addition to transversely isotropic models) and found that the deviations from ray theoretical predictions are more pronounced at certain azimuths for this symmetry class.

There are several potential reasons for the (generally relatively minor) deviations between the synthetic splitting results and the ray theoretical predictions for our upper mantle models. The most important one is that AxiSEM3D considers full wave sensitivity to Earth structure and accounts for finite frequency effects, in contrast to ray theoretical methods. Other effects may include the fact that the ray theoretical calculations are based on a geometrical approximation of the path of the seismic ray travelling through an average, depth-weighted elasticity tensor; in AxiSEM3D, the elasticity is discretized in 33 different layers and varies with depth. Finally, like Lin *et al.* (2014a,b) we also noted some complexities in the apparent splitting parameters due to interference with other seismic phases that could perturb the splitting measurement. This phenomenon is particularly recognizable in the HTI case, where a second wiggle is very close to the *SKKS* phase, especially in the $30-60^{\circ}$ ($120-150^{\circ}$) backazimuthal ranges (Fig. 6) and it can also be observed in the upper mantle orthorombic case at 45° (Fig. 10). These other seismic phases coming in between *SKS* and *SKKS* correspond to *PPPP* phases: it can be observed from the seismograms directly that this phase is not split (no energy on the transverse component), consistent with it being a *P* phase. The amplitude of this phase is strongly attenuated in real data seismograms, but since attenuation is turned off in our simulations they show up with high amplitude in our synthetics.

In general, while ray theory is generally an adequate approximation for *SK*(*K*)*S* splitting due to upper mantle anisotropy, it is more likely to be inadequate when the anisotropic models under study are complicated (either in terms of their symmetry, as in this study, or when there are lateral variations in anisotropic structure, which was not considered here but which will be considered in future works). Similar to Lin *et al.* (2014a), we found that modest differences in splitting intensity for *SKS* versus *SKKS* phases (up to $\sim$0.2 s, with values up to $\sim$0.4 s for specific symmetries and at certain azimuths) for the same event-station pair can be caused by waveform effects for models that include upper mantle anisotropy only. We note, however, that the *SKS*−*SKKS* discrepancies due to upper mantle anisotropy documented in this study are modest compared to the larger discrepancies observed for the lowermost mantle cases (Section 5). For example, for the bridgmanite case, discrepancies larger than 0.5 s and up to $\sim$1 s are observed in the $30-75^{\circ}$ ($105-135^{\circ}$) backazimuthal range (Fig. 11), while discrepancies as high as $\sim$2.5 s are obtained for post-perovskite models (Fig. 13). Our findings reinforce the need for *SKS*−*SKKS* discrepancy studies of mantle anisotropy to exercise caution when interpreting weakly discrepant splitting, and to only attribute strong differences in splitting intensity values to anisotropy in the lowermost mantle (e.g. Deng *et al.* 2017; Reiss *et al.* 2019).

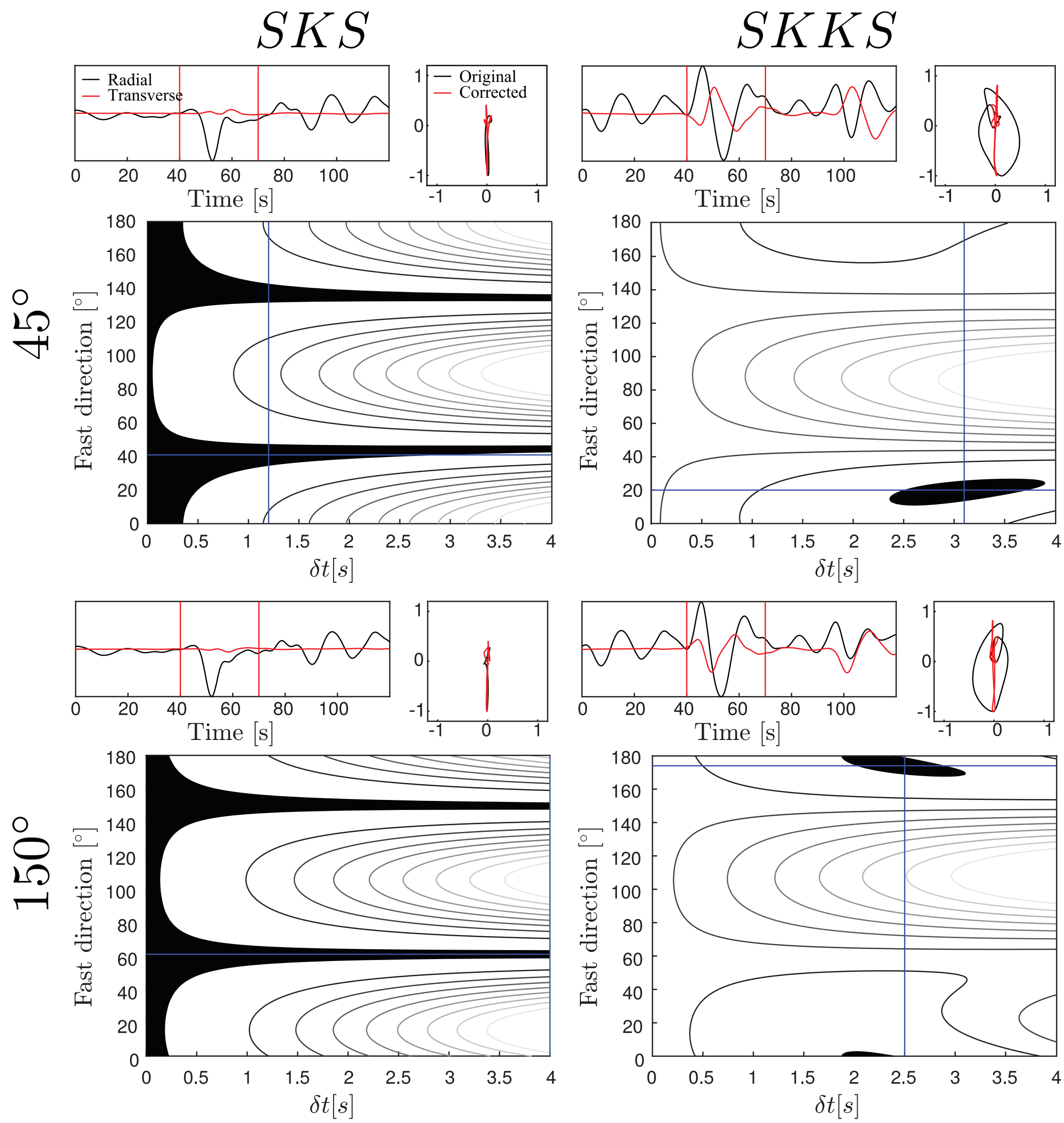

Figure 14. Same as Fig. 8 but with the anisotropy localized in a 250-km-thick D'' layer. The elasticity tensor used for this test is the one shown in Fig. 4, bottom row. Also in this case we note a strong discrepancies between *SKS* and *SKKS*, with the *SKS* yielding null measurements.

For the lower mantle, our results have shown that lowermost mantle anisotropy can have a significant effect on the splitting of *SKS* and *SKKS* phases, in agreement with the sensitivity kernel computations of Zhao & Chevrot (2011). A comparison between our shear wave splitting measurements on synthetic waveforms and the predictions of ray theory (for models that represent bridgmanite and post-perovskite elasticity) reveals that, as for the upper mantle models, ray theory generally correctly captures the first-order aspects of the splitting behaviour. However, ray theory typically slightly overpredicts the magnitude of shear wave splitting when compared to the behaviour of the full waveform. From these results, we conclude that forward modelling approaches for lowermost mantle anisotropy models that rely on ray theory (e.g. Walker *et al.* 2011; Cottaar *et al.* 2014; Ford *et al.* 2015; Ford & Long 2015; Creasy *et al.* 2017, 2019; Tommasi *et al.* 2018) are generally valid, but are less accurate than full-wavefield simulations. This implies that moving to approaches that consider the full waveform behaviour is desirable in future modelling work aimed at D'' anisotropy problems, as also suggested by Nowacki & Wookey (2016).

7.3 Limitations and future work

While this study has established the feasibility of full-wave solutions using AxiSEM3D for earth models that include anisotropy of arbitrary symmetry, it is important to highlight some caveats and limitations. One area in which particular concern must be taken in future studies of mantle anisotropy has to do with the design of the mesh and the size of anisotropic regions. In spectral element methods, the domain is subdivided into a number of non-overlapping quadrangular shaped elements, and on each element the nodes are chosen to be the Gauss–Lobatto–Legendre (GLL) points where the wave equation is evaluated (Peter *et al.* 2011). A good mesh design

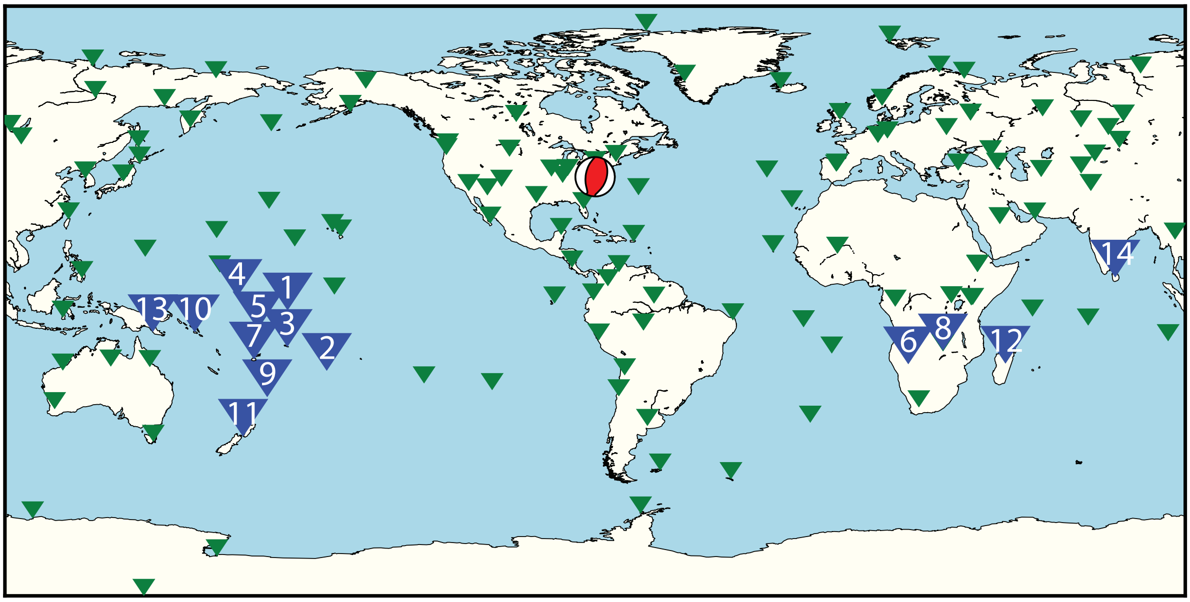

Figure 15. Source and receiver configuration for the AxiSEM3D-SPECFEM3D_GLOBE cross-verification exercise. The earthquake source is located in Virginia, US (37.91°N, 77.93°W), at a depth of 12 km (event ID 201108231751A). Receivers of the Global Seismographic Network (GSN) are shown as green triangles. The large blue triangles with numbers are 14 representative stations where the synthetic seismograms displayed in Fig. 16 are computed.

must consider this characteristic and allow for seismic discontinuities to lie on the GLL points. This will make sure that the points at the discontinuity have the elastic properties of both materials, which in turn will allow for the correct partitioning of seismic energy at the interface and avoid contamination of the numerical solution by artefacts due to staircase sampling effects. A proper mesh design is an essential requirement for all spectral element methods and not just AxiSEM3D. It is indeed a more complex task to achieve for 3-D discrete methods as 3-D meshes that honour these conditions have to be generated, while for AxiSEM3D this condition applies to 2-D meshes. With this in mind, in future studies that interrogate anisotropic earth models, it will be important to ensure that anisotropic discontinuities are also honoured by the mesh design. This is relatively easy to accomplish in the case of vertical stratification of anisotropy (that is, horizontal interfaces), but it turns out to be more complex for cases of lateral variation in anisotropic properties, which are likely relevant for many regions of the Earth.

Consideration of laterally heterogeneous anisotropic structures has been intentionally neglected in this study, whose main purposes are to establish AxiSEM3D as a tool for modelling seismic waveforms in arbitrary anisotropic global earth models and to interrogate the behaviour of relatively simple anisotropy scenarios. However, more realistic models that include lateral heterogeneity are needed to more fully explore the origin of *SKS*−*SKKS* splitting discrepancies and the possible contributions of lowermost mantle anisotropy to *SK*(*K*)*S* phases in the real Earth. This is particularly true given that in the lowermost mantle, the length scale of anisotropic heterogeneity may be smaller than the Fresnel zone of *SK*(*K*)*S* phases; in practice, therefore, it is not clear how large the contribution to *SK*(*K*)*S* splitting may be for realistic models of lowermost mantle anisotropy. Now that AxiSEM3D has been established as a computationally efficient tool for modelling wave propagation in an anisotropic Earth, work to understand the full-wave sensitivity of *SK*(*K*)*S* phases to anisotropy in more realistic, heterogeneous Earth models is ongoing. In the case of 1-D anisotropic models, such as those considered in this study, the Fourier spectral order required for a correct approximate solution to the 3-D wave equation is dependent on the complexities of the underlying seismic velocity model. For a fully 3-D anisotropic model, it is crucial to ensure that the Fourier spectral order of expansion is large enough to correctly account for the geometrical properties of the anisotropic model. As the cost of 3-D anisotropic wavefield simulations increase with growing Fourier order, careful attention must be paid to the geographic dimensions of anisotropic domains in 3-D models in order to preserve the computational advantages of the method with respect to 3-D discrete spectral element methods.

7.4 Implications for the interpretation of *SKS*−*SKKS* splitting discrepancies

Observations of discrepant *SKS*−*SKKS* splitting for pairs of phases from the same event-station pair have been puzzling to shear wave splitting analysts since they were first documented by James & Assumpção (1996). A global study by Niu & Perez (2004) found that 95 per cent of *SKS*−*SKKS* observations globally were non-discrepant; that is, the *SKS* and *SKKS* phases showed similar splitting behaviour. In the remaining 5 per cent of cases, however, the pairs exhibited discrepant splitting. Niu & Perez (2004) argued that because *SKS* and *SKKS* phases have nearly identical ray paths in the upper mantle but diverge significantly in the lower mantle, discrepancies in *SKS*−*SKKS* splitting should be attributed to anisotropy in the lower mantle. Restivo & Helffrich (2006) suggested that anisotropy in the D'' layer is the most likely explanation for such discrepancies, and argued that topography on structures at or near the CMB may generate polarization anomalies, and thus splitting anomalies. A key aspect of the argument made by Restivo & Helffrich (2006) is that lateral gradients in structure at the base of the mantle are responsible for *SKS*−*SKKS* splitting discrepancies. This notion was invoked by subsequent studies of *SKS*−*SKKS* splitting discrepancies and lowermost mantle structure (e.g. Wang & Wen

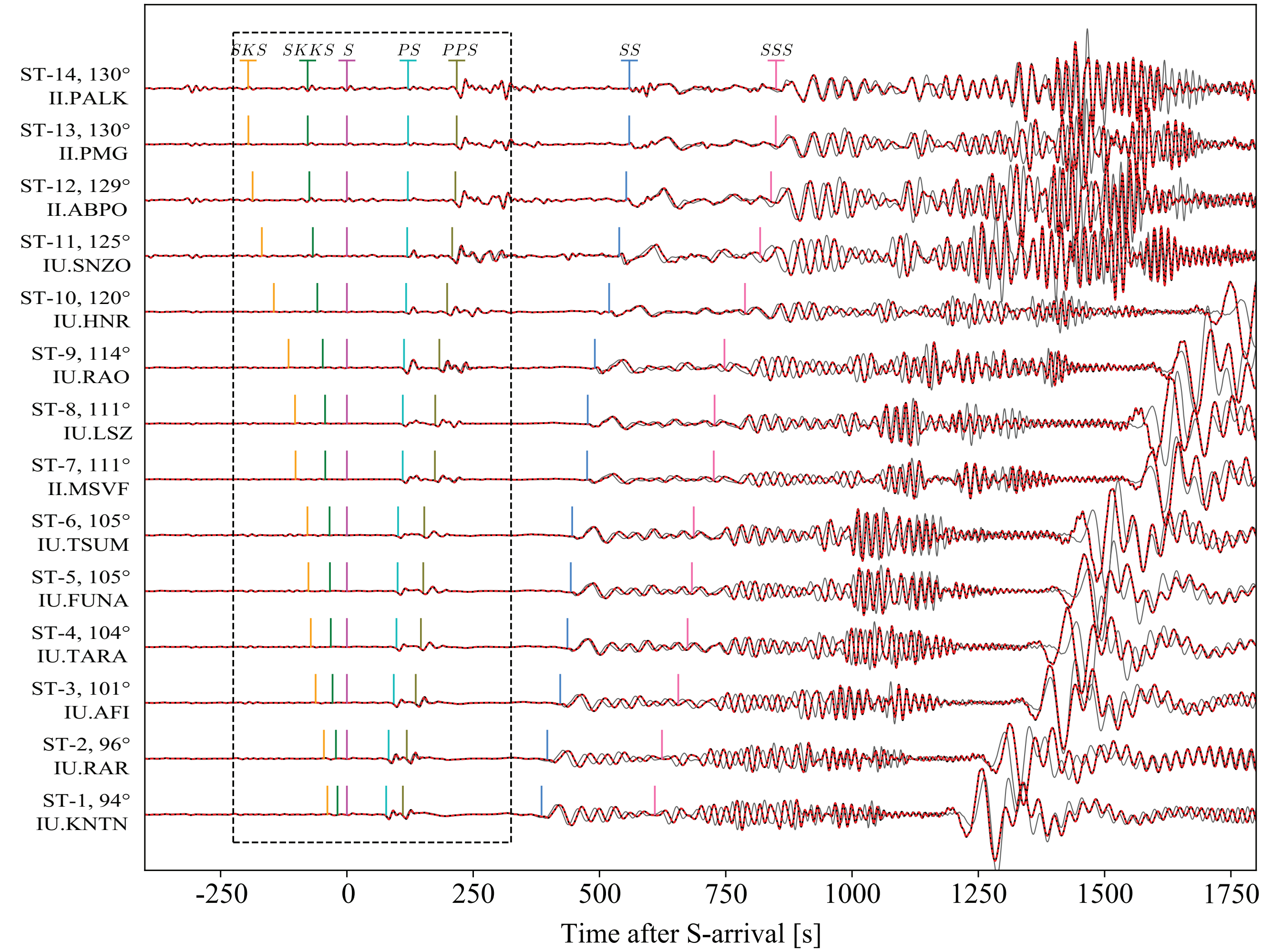

Figure 16. Comparison of synthetic waveforms computed by SPECFEM3D_GLOBE (black) and AxiSEM3D (dashed red) for the tomographic model of Montagner (2002), which includes 3-D anisotropy. Synthetic seismograms for the radially anisotropic PREM model are shown in light grey for comparison. We show vertical displacements for all three cases. The receiver locations are shown with blue triangles in Fig. 15. Radial and transverse components are shown in Fig. 17 in the time-window bounded by the dashed black line that includes *SKS* and *SKKS* phases.

2007; Long 2009), who argued that *SKS*−*SKKS* splitting discrepancies should be interpreted in terms of a lateral gradient in seismic anisotropy at the base of the mantle (that is, with the *SKS* and *SKKS* phases sampling a different geometry and/or strength of lowermost mantle anisotropy). More recent papers that have been informed by forward modelling studies (e.g. Ford *et al.* 2015; Creasy *et al.* 2019) have explicitly acknowledged the possibility that *SKS*−*SKKS* splitting discrepancies can arise from homogenous anisotropy at the base of the mantle (e.g. Long & Lynner 2015; Deng *et al.* 2017; Wolf *et al.* 2019; Reiss *et al.* 2019). In this case, the anisotropy must be present in a geometry that splits *SKS* and *SKKS* phases differently.

While many authors have interpreted *SKS*−*SKKS* splitting discrepancies as reflecting a contribution from anisotropy in the lower(most) mantle, other workers have questioned the extent to which anisotropy in the upper mantle may give rise to such discrepancies (or to discrepancies in splitting between *SKS* phases measured at the same station at similar backazimuths and incidence angles). For example, Monteiller & Chevrot (2010) documented differences in transverse component waveforms for pairs of *SKS* and *SKKS* phases from nearby earthquakes, and pointed out that the variability between phases coming from nearby directions is of similar magnitude to the variability documented in previous studies of*SKS*−*SKKS* splitting discrepancies that invoked D'' anisotropy as an explanation. Monteiller & Chevrot (2010) suggested that noise on the transverse component waveforms was the most likely explanation for these discrepancies, although other workers have argued that strong discrepancies measured on seismograms with relatively low noise levels cannot be due (solely) to noise (Long 2009; Lynner & Long 2014; Long & Lynner 2015). In a later paper, Monteiller & Chevrot (2011) documented differences in estimated *SKS* splitting parameters for stations in southern California between their measurements, obtained with the splitting intensity method, and previously published measurements; again, they attributed these discrepancies to the presence of noise and to differences in processing and measurement methods. Finally, Lin *et al.* (2014a) showed that full-wave effects can cause splitting discrepancies between *SKS* and *SKKS* phases for the same event-station pairs of up to ∼0.3 s at certain azimuths for models that only include homogeneous upper mantle anisotropy, as discussed in Section 4.1.

What insights do our simulations give us into the interpretations of *SKS*−*SKKS* splitting discrepancies? Our documentation of

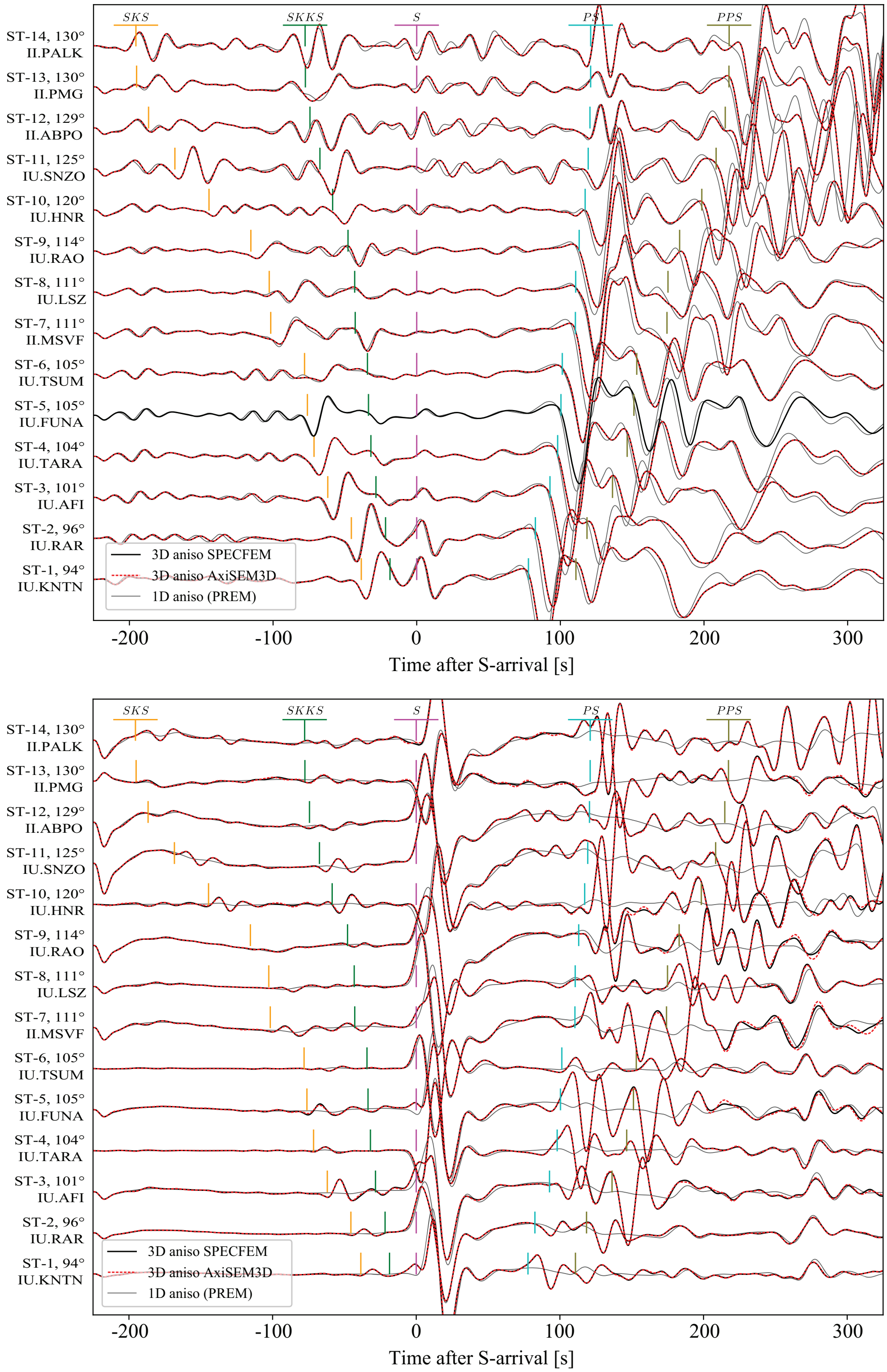

Figure 17. Details of the radial (top panel) and transverse (bottom panel) components of the synthetic waveforms presented in Fig. 16. Both AxiSEM3D (dashed red) and SPECFEM3D_GLOBE (black) waveforms show clear evidence of splitting energy between radial and transverse components as a function of the backazimuth.

predicted *SKS*−*SKKS* splitting discrepancies for both upper and lowermost mantle anisotropy models demonstrates that such discrepancies can arise from a physical cause, although of course the effects of noise must be considered for actual data. Similar to Lin *et al.* (2014a), we found that modest splitting intensity discrepancies (typically up to 0.2 s, with a few values up to 0.4 s) can arise from homogeneous upper mantle anisotropy models, possibly influenced by the interference of other phases in the

SK(*K*)*S* time window. Our simulations showed that much larger *SKS*−*SKKS* splitting intensity discrepancies can arise from lowermost mantle anisotropy models (up to ∼1.0 s or greater for post-perovskite; see Fig. 13). Therefore, our work shows that both upper and lowermost mantle anisotropy may potentially contribute to *SKS*−*SKKS* splitting intensity discrepancies for simple, homogeneous anisotropic models. Ongoing work that extends to models that include realistic 3-D heterogeneity in anisotropic structure will answer the question of whether our general finding that lowermost mantle anisotropy models predict substantially stronger *SKS*−*SKKS* splitting discrepancies than upper mantle models holds for more complex models. Particularly because *SK*(*K*)*S* phases have large zones of sensitivity at the base of the mantle (e.g. Zhao & Chevrot 2011), and because there may be heterogeneity in lowermost mantle anisotropy on length scales shorter than the Fresnel zones of the *SK*(*K*)*S* waves under study, lowermost mantle anisotropy may contribute less to the splitting of *SK*(*K*)*S* phases in practice than the results from laterally homogeneous models suggest. Furthermore, for actual, noisy data that reflects complex Earth structure, the effects of noise, phase interference, and complex wave propagation effects on apparent splitting parameters must be carefully considered.

Our lowermost mantle simulations also reinforce the notion that discrepant splitting behaviour between *SKS* and *SKKS* phases can arise even in models that feature laterally homogeneous anisotropic structure in the lowermost mantle. While *SKS* − *SKKS* splitting discrepancies are often taken to imply a lateral gradient in anisotropy between the respective D'' pierce points of the *SKS* and *SKKS* phases (e.g. Long 2009), our simulations (and previous work by others, including work based on ray theoretical approximations) show that homogeneous anisotropy can give rise to such discrepancies. *SKS*−*SKKS* splitting discrepancies, when interpreted in the context of lowermost mantle anisotropy, should therefore be taken to imply a contribution to splitting from anisotropy sampled by one or both phases (e.g. Lynner & Long 2014; Long & Lynner 2015; Deng *et al.* 2017; Reiss *et al.* 2019), rather than to require a lateral gradient in D'' anisotropy.

8 CONCLUSION

We have presented a new wavefield modelling strategy to introduce the effects of general anisotropy in global models using the pseudospectral element code AxiSEM3D. The implementation of arbitrary anisotropy is accomplished by describing the elastic properties of the seismic domain in terms of the full elastic tensor with 21 independent coefficients. We have carried out global wavefield simulations for models that include anisotropy in the upper and lowermost mantle, reaching frequencies as high as 0.2 Hz with relatively modest computational resources. We benchmarked our implementation against known reference solutions for simple upper mantle models, and then investigated the behaviour of *SK*(*K*)*S* phases for models that include upper mantle anisotropy (in HTI and orthorhombic geometries) as well as those that include anisotropy at the base of the mantle (for possible bridgmanite and post-perovskite CPO scenarios). We carried out shear wave splitting analysis (both the traditional transverse component minimization method and the splitting intensity method) on synthetic waveforms for the suite of global anisotropic models. These tests revealed that shear wave splitting, as manifested in the full-wavefield simulations, behaves similarly to the predictions of ray theory to first order, but some departures from ray theoretical behaviour (due to full waveform effects) are found. Our results indicate that although some *SKS*−*SKKS* splitting intensity discrepancies arise from anisotropic upper mantle models, particularly when low symmetry classes (e.g. orthorhombic) are considered, these are of modest amplitude (generally less than 0.2 s, with a few discrepancies up to 0.4 s). On the other hand, we find that realistic lowermost mantle anisotropy scenarios can cause significant splitting (up to ∼1 s) of *SK*(*K*)*S* waveforms when full wave propagation is taken into account, with *SKS*−*SKKS* splitting intensity discrepancies up to ∼1 s or greater. The cross-validation test with the discrete spectral element solver SPECFEM3D_GLOBE further highlights the capability of AxiSEM3D to handle increasingly complex earth models, including those with arbitrary anisotropic symmetry, without loss of accuracy and with accessible computing resources. In the future, AxiSEM3D will be used to investigate the behaviour of *SK*(*K*)*S* phases in the presence of lateral heterogeneity in anisotropic structure, paving the way for more realistic consideration of full wavefield effects when interpreting shear wave splitting measurements, particularly due to D'' anisotropy.

ACKNOWLEDGEMENTS

We are grateful to Neala Creasy and Miriam Reiss for fruitful discussions and assistance with shear wave splitting measurements. We thank Vadim Levin and the Rutgers University seismology group for insightful discussions that helped lead us to our modelling strategy. We thank Andy Nowacki for sharing his code and providing detailed instructions to help us understand the implementation of full anisotropy in SPECFEM3D_GLOBE. We thank the Yale Center for Research Computing for guidance and use of the research computing infrastructure, specifically the Grace cluster. We also acknowledge use of the U.K. supercomputer ARCHER. We are also grateful to the editor, Professor Li Zhao, and another reviewer for their constructive comments that helped us improve our manuscript. This work was funded by the U.S. National Science Foundationvia grant EAR-1547499 to MDL. KL and TNM acknowledge support by NERC Grant NE/R012199/1. For the collaboration of this work, KL worked as a postdoctoral associate at Yale University, funded via NSF grant EAR-1610612 to Jun Korenaga.

REFERENCES

Abramson, E.H., Brown, J.M., Slutsky, L.J. & Zaug, J., 1997. The elastic constants of San Carlos olivine to 17 GPa, *J. geophys. Res.,* **102**(B6), 12 253–12 263.

Anderson, D., 1989. *Theory of the Earth,* Blackwell Science.

Anderson, D.L., 1961. Elastic wave propagation in layered anisotropic media, *J. geophys. Res.,* **66**(9), 2953–2963.

Anderson, D.L. & Dziewonski, A.M., 1982. Upper mantle anisotropy: evidence from free oscillations, *J. geophys. Int.,* **69**(2), 383–404.

Auer, L., Boschi, L., Becker, T.W., Nissen-Meyer, T. & Giardini, D., 2014. Savani: a variable resolution whole-mantle model of anisotropic shear velocity variations based on multiple data sets, *J. geophys. Res.,* **119**(4), 3006–3034.

Babuska, V. & Cara, M., 1991. *Seismic Anisotropy in the Earth,* 1st edn, Springer Netherlands.

Barruol, G. & Kern, H., 1996. Seismic anisotropy and shear-wave splitting in lower-crustal and upper-mantle rocks from the Ivrea Zone—experimental and calculated data, *Phys. Earth planet. Inter.,* **95**(3–4), 175–194.

Becker, T.W., Chevrot, S., Schulte-Pelkum, V. & Blackman, D.K., 2006. Statistical properties of seismic anisotropy predicted by upper mantle geodynamic models, *J. geophys. Res.,* **111**(B8), doi:10.1029/2005JB004095.

Beghein, C. & Trampert, J., 2003. Robust normal mode constraints on inner-core anisotropy from model space search, *Science,* **299**(5606), 552–555.

Beghein, C., Resovsky, J. & van der Hilst, R.D., 2008. The signal of mantle anisotropy in the coupling of normal modes, *J. geophys. Int.,* **175**(3), 1209–1234.

Ben Ismaïl, W. & Mainprice, D., 1998. An olivine fabric database: an overview of upper mantle fabrics and seismic anisotropy, *Tectonophysics,* **296**(1–2), 145–157.

Browaeys, J.T. & Chevrot, S., 2004. Decomposition of the elastic tensor and geophysical applications, *J. geophys. Int.,* **159**(2), 667–678.

Buehler, J.S. & Shearer, P.M., 2017. Uppermost mantle seismic velocity structure beneath USArray, *J. geophys. Res.,* **122**(1), 436–448.

Chevrot, S., 2000. Multichannel analysis of shear wave splitting, *J. geophys. Res.,* **105**(B9), 21 579–21 590.

Chevrot, S., 2006. Finite-frequency vectorial tomography: a new method for high-resolution imaging of upper mantle anisotropy, *J. geophys. Int.,* **165**(2), 641–657.

Cottaar, S. & Romanowicz, B., 2013. Observations of changing anisotropy across the southern margin of the African LLSVP, *J. geophys. Int.,* **195**(2), 1184–1195.

Cottaar, S., Li, M., McNamara, A.K., Romanowicz, B. & Wenk, H.-R., 2014. Synthetic seismic anisotropy models within a slab impinging on the core–mantle boundary, *J. geophys. Int.,* **199**(1), 164–177.

Creasy, N., Long, M.D. & Ford, H.A., 2017. Deformation in the lowermost mantle beneath Australia from observations and models of seismic anisotropy, *J. geophys. Res.,* **122,** (7), 5243–5267.

Creasy, N., Pisconti, A., Long, M.D., Thomas, C. & Wookey, J., 2019. Constraining lowermost mantle anisotropy with body waves: a synthetic modelling study, *J. geophys. Int.,* **217**(2), 766–783.

Crotwell, H.P., Owens, T.J. & Ritsema, J., 1999. The TauP toolkit: flexible seismic travel-time and ray-path utilities, *Seismol. Res. Lett.,* **70,** 154–160.

Deng, J., Long, M.D., Creasy, N., Wagner, L., Beck, S., Zandt, G., Tavera, H. & Minaya, E., 2017. Lowermost mantle anisotropy near the eastern edge of the Pacific LLSVP: constraints from SKS-SKKS splitting intensity measurements, *J. geophys. Int.,* **210**(2), 774–786.

Dziewonski, A.M. & Anderson, D.L., 1981. Preliminary reference Earth model, *Phys. Earth planet. Inter.,* **25**(4), 297–356.

Eakin, C.M. & Long, M.D., 2013. Complex anisotropy beneath the peruvian flat slab from frequency-dependent, multiple-phase shear wave splitting analysis, *J. geophys. Res.,* **118**(9), 4794–4813.

Favier, N. & Chevrot, S., 2003. Sensitivity kernels for shear wave splitting in transverse isotropic media, *J. geophys. Int.,* **153**(1), 213–228.

Favier, N., Chevrot, S. & Komatitsch, D., 2004. Near-field influence on shear wave splitting and traveltime sensitivity kernels, *J. geophys. Int.,* **156**(3), 467–482.

Ferreira, A. M.G., Faccenda, M., Sturgeon, W., Chang, S.-J. & Schardong, L., 2019. Ubiquitous lower-mantle anisotropy beneath subduction zones, *Nat. Geosci.,* **12**(4), 301–306.

Foley, B.J. & Long, M.D., 2011. Upper and mid-mantle anisotropy beneath the Tonga slab, *Geophys. Res. Lett.,* **38**(2), doi:10.1029/2010GL046021.

Ford, H.A. & Long, M.D., 2015. A regional test of global models for flow, rheology, and seismic anisotropy at the base of the mantle, *Phys. Earth planet. Inter.,* **245,** 71–75.

Ford, H.A., Long, M.D., He, X. & Lynner, C., 2015. Lowermost mantle flow at the eastern edge of the African large low shear velocity province, *Earth planet. Sci. Lett.,* **420,** 12–22.

Forsyth, D.W., 1975. The early structural evolution and anisotropy of the oceanic upper mantle, *J. geophys. Int.,* **43**(1), 103–162.

Grund, M. & Ritter, J.R.R., 2018. Widespread seismic anisotropy in Earth's lowermost mantle beneath the Atlantic and Siberia, *Geology,* **47**(2), 123–126.

He, X. & Long, M.D., 2011. Lowermost mantle anisotropy beneath the northwestern Pacific: evidence from PcS, ScS, SKS, and SKKS phases, *Geochem. Geophys. Geosyst.,* **12**(12), doi:10.1029/2011GC003779

Hernlund, J.W., Thomas, C. & Tackley, P.J., 2005. A doubling of the post-perovskite phase boundary and structure of the earth's lowermost mantle, *Nature,* **434**(7035), 882–886.

Hess, H.H., 1964. Seismic anisotropy of the uppermost mantle under oceans, *Nature,* **203**(4945), 629–631.

Houser, C., 2007. Constraints on the presence or absence of post-perovskite in the lowermost mantle from long-period seismology, in *Geophysical Monograph Series,* pp. 191–216, American Geophysical Union.

Isaak, D.G., 1992. High-temperature elasticity of iron-bearing olivines, *J. geophys. Res.,* **97**(B2), 1871–1885.

Jaeken, J.W. & Cottenier, S., 2016. Solving the Christoffel equation: phase and group velocities, *Comp. Phys. Commun.,* **207,** 445–451.

James, D.E. & Assumpção, M., 1996. Tectonic implications of S-wave anisotropy beneath SE Brazil, *J. geophys. Int.,* **126**(1), 1–10.

Karato, S., Jung, H., Katayama, I. & Skemer, P., 2008. Geodynamic significance of seismic anisotropy of the upper mantle: new insights from laboratory studies, *Ann. Rev. Earth Planet. Sci.,* **36**(1), 59–95.

Koelemeijer, P., Schuberth, B.S.A., Davies, D.R., Deuss, A. & Ritsema, J., 2018. Constraints on the presence of post-perovskite in Earth's lowermost mantle from tomographic-geodynamic model comparisons, *Earth planet. Sci. Lett.,* **494,** 226–238.

Komatitsch, D. & Tromp, J., 2002a. Spectral-element simulations of global seismic wave propagation — I. Validation, *J. geophys. Int.,* **149**(2), 390–412.

Komatitsch, D. & Tromp, J., 2002b. Spectral-element simulations of global seismic wave propagation—II. Three-dimensional models, oceans, rotation and self-gravitation, *J. geophys. Int.,* **150**(1), 303–318.

Leng, K., Nissen-Meyer, T. & van Driel, M., 2016. Efficient global wave propagation adapted to 3-D structural complexity: a pseudospectral/spectral-element approach, *J. geophys. Int.,* **207**(3), 1700–1721.

Leng, K., Nissen-Meyer, T., van Driel, M., Hosseini, K. & Al-Attar, D., 2019. AxiSEM3D: broad-band seismic wavefields in 3-D global earth models with undulating discontinuities, *J. geophys. Int.,* **217**(3), 2125–2146.

Levin, V. & Park, J., 1998. P-SH conversions in layered media with hexagonally symmetric anisotropy: a cookbook, *Pure appl. Geophys.,* **151**(2–4), 669–697.

Levin, V., Menke, W. & Park, J., 1999. Shear wave splitting in the Appalachians and the Urals: a case for multilayered anisotropy, *J. geophys. Res.,* **104**(B8), 17 975–17 993.

Lin, Y.-P., Zhao, L. & Hung, S.-H., 2014a. Full-wave effects on shear wave splitting, *Geophys. Res. Lett.,* **41**(3), 799–804.

Lin, Y.-P., Zhao, L. & Hung, S.-H., 2014b. Full-wave multiscale anisotropy tomography in Southern California, *Geophys. Res. Lett.,* **41**(24), 8809–8817.

Long, M.D., 2009. Complex anisotropy in D$''$ beneath the Eastern Pacific from SKS–SKKS splitting discrepancies, *Earth planet. Sci. Lett.,* **283**(1-4), 181–189.

Long, M.D., 2013. Constraints on subduction geodynamics from seismic anisotropy, *Rev. Geophys.,* **51**(1), 76–112.

Long, M.D. & Becker, T.W., 2010. Mantle dynamics and seismic anisotropy, *Earth planet. Sci. Lett.,* **297,** 341–354.

Long, M.D. & Lynner, C., 2015. Seismic anisotropy in the lowermost mantle near the Perm anomaly, *Geophys. Res. Lett.,* **42**(17), 7073–7080.

Long, M.D. & Silver, P.G., 2009. Shear wave splitting and mantle anisotropy: measurements, interpretations, and new directions, *Surv. Geophys.,* **30**(4–5), 407–461.

Long, M.D. & van der Hilst, R.D., 2005. Estimating shear-wave splitting parameters from broadband recordings in Japan: a comparison of three methods, *Bull. seism. Soc. Am.,* **95**(4), 1346–1358.

Long, M.D., de Hoop, M.V. & van der Hilst, R.D., 2008. Wave-equation shear wave splitting tomography, *J. geophys. Int.,* **172**(1), 311–330.

Lynner, C. & Long, M.D., 2014. Lowermost mantle anisotropy and deformation along the boundary of the African LLSVP, *Geophys. Res. Lett.,* **41**(10), 3447–3454.

Lynner, C. & Long, M.D., 2015. Heterogeneous seismic anisotropy in the transition zone and uppermost lower mantle: evidence from South America, Izu-Bonin and Japan, *J. geophys. Int.,* **201**(3), 1545–1552.

Malvern, L.E., 1969. *Introduction to the Mechanics of a Continuous Medium,* Pearson.

Mao, Z., Fan, D., Lin, J.-F., Yang, J., Tkachev, S.N., Zhuravlev, K. & Prakapenka, V.B., 2015. Elasticity of single-crystal olivine at high pressures and temperatures, *Earth planet. Sci. Lett.,* **426,** 204–215.

Marson-Pidgeon, K. & Savage, M.K., 2004. Modelling shear wave splitting observations from Wellington, New Zealand, *J. geophys. Int.,* **157**(2), 853–864.

Mondal, P. & Long, M.D., 2019. A model space search approach to finite-frequency SKS splitting intensity tomography in a reduced parameter space, *J. geophys. Int.,* **217**(1), 238–256.

Montagner, J.P., 2002. Upper mantle low anisotropy channels below the Pacific Plate, *Earth planet. Sci. Lett.,* **202**(2), 263–274.

Monteiller, V. & Chevrot, S., 2010. How to make robust splitting measurements for single-station analysis and three-dimensional imaging of seismic anisotropy *Geophys. J. Int.* **182 ,** (1), 311–328.

Monteiller, V. & Chevrot, S., 2011. High-resolution imaging of the deep anisotropic structure of the San Andreas fault system beneath Southern California, *J. geophys. Int.,* **186**(2), 418–446.

Moulik, P. & Ekström, G., 2014. An anisotropic shear velocity model of the Earth's mantle using normal modes, body waves, surface waves and long-period waveforms, *J. geophys. Int.,* **199**(3), 1713–1738.

Murakami, M., Hirose, K., Kawamura, K., Sata, N. & Ohishi, Y., 2004. Post-perovskite phase transition in $MgSiO_3$, *Science,* **304**(5672), 855–858.

Nissen-Meyer, T., van Driel, M., Sthler, S.C., Hosseini, K., Hempel, S., Auer, L., Colombi, A. & Fournier, A., 2014. AxiSEM: broadband 3-D seismic wavefields in axisymmetric media, *Solid Earth,* **5**(1), 425–445.

Niu, F. & Perez, A.M., 2004. Seismic anisotropy in the lower mantle: a comparison of waveform splitting of SKS and SKKS, *Geophys. Res. Lett.,* **31**(24), doi:10.1029/2004GL021196.

Nowacki, A. & Wookey, J., 2016. The limits of ray theory when measuring shear wave splitting in the lowermost mantle with ScS waves, *J. geophys. Int.,* **207**(3), 1573–1583.

Nowacki, A., Wookey, J. & Kendall, J.-M., 2010. Deformation of the lowermost mantle from seismic anisotropy, *Nature,* **467**(7319), 1091–1094.

Nowacki, A., Wookey, J. & Kendall, J.-M., 2011. New advances in using seismic anisotropy, mineral physics and geodynamics to understand deformation in the lowermost mantle, *J. Geodyn.,* **52**(3-4), 205–228.

Park, J. & Yu, Y., 1993. Seismic determination of elastic anisotropy and mantle flow, *Science,* **261**(5125), 1159–1162.

Peter, D. *et al.*, 2011. Forward and adjoint simulations of seismic wave propagation on fully unstructured hexahedral meshes, *J. geophys. Int.,* **186**(2), 721–739.

Rao, B.P., Kumar, M.R. & Singh, A., 2017. Anisotropy in the lowermost mantle beneath the Indian Ocean Geoid Low from ScS splitting measurements, *Geochem. Geophys. Geosyst.,* **18**(2), 558–570.

Reiss, M., Long, M. & Creasy, N., 2019. Lowermost mantle anisotropy beneath africa from differential SKS-SKKS shear-wave splitting, *J. geophys. Res.,* **124** (8), 8540–8564.

Reiss, M.C. & Rümpker, G., 2017. SplitRacer: MATLAB code and GUI for semiautomated analysis and interpretation of teleseismic shear-wave splitting, *Seismol. Res. Lett.,* **88**(2A), 392–409.

Restivo, A. & Helffrich, G., 2006. Core-mantle boundary structure investigated SKS and SKKS polarization anomalies, *J. geophys. Int.,* **165**(1), 288–302.

Ritsema, J., Deuss, A., van Heijst, J. & Woodhouse, J.H., 2011. S40RTS: a degree-40 shear-velocity model for the mantle from new Rayleigh wave dispersion, teleseismic traveltime and normal-mode splitting function measurements, *J. geophys. Int.,* **184**(3), 1223–1236.

Roy, S.K., Ravi Kumar, M. & Srinagesh, D., 2014. Upper and lower mantle anisotropy inferred from comprehensive SKS and SKKS splitting measurements from India, *Earth planet. Sci. Lett.,* **392,** 192–206.

Savage, M.K., 1999. Seismic anisotropy and mantle deformation: what have we learned from shear wave splitting? *Rev. Geophys.,* **37**(1), 65–106.

Schaeffer, A.J., Lebedev, S. & Becker, T.W., 2016. Azimuthal seismic anisotropy in the Earth's upper mantle and the thickness of tectonic plates, *J. geophys. Int.,* **207**(2), 901–933.

Schulte-Pelkum, V., Masters, G. & Shearer, P.M., 2001. Upper mantle anisotropy from long-period P polarization, *J. geophys. Res.,* **106**(B10), 21 917–21 934.

Servali, A., Long, M.D., Park, J., Benoit, M.H. & Aragon, J.C., 2020. Love-to-Rayleigh scattering across the eastern North American passive margin, *Tectonophysics,* **776,** 228321.

Sieminski, A., Paulssen, H., Trampert, J. & Tromp, J., 2008. Finite-frequency SKS splitting: measurement and sensitivity kernels, *Bull. seism. Soc. Am.,* **98**(4), 1797–1810.

Silver, P.G., 1996. Seismic anisotropy beneath the continents: probing the depths of geology, *Ann. Rev. Earth planet. Sci.,* **24,** 385–432.

Silver, P.G. & Chan, W.W., 1988. Implications for continental structure and evolution from seismic anisotropy, *Nature,* **335**(6185), 34–39.

Silver, P.G. & Chan, W.W., 1991. Shear wave splitting and subcontinental mantle deformation, *J. geophys. Res.,* **96**(B10), 16 429–16 454.

Silver, P.G. & Savage, M.K., 1994. The interpretation of shear-wave splitting parameters in the presence of two anisotropic layers, *J. geophys. Int.,* **119**(3), 949–963.

Skemer, P. & Hansen, L.N., 2016. Inferring upper-mantle flow from seismic anisotropy: an experimental perspective, *Tectonophysics,* **668-669,** 1–14.

Tesoniero, A., Auer, L., Boschi, L. & Cammarano, F., 2015. Hydration of marginal basins and compositional variations within the continental lithospheric mantle inferred from a new global model of shear and compressional velocity, *J. geophys. Res.,* **120**(11), 7789–7813.

Tommasi, A., Goryaeva, A., Carrez, P., Cordier, P. & Mainprice, D., 2018. Deformation, crystal preferred orientations, and seismic anisotropy in the Earth's D'' layer, *Earth planet. Sci. Lett.,* **492,** 35–46.

Tromp, J., 1995. Normal-mode splitting due to inner-core anisotropy, *J. geophys. Int.,* **121**(3), 963–968.

Vinnik, L.P., Farra, V. & Romanowicz, B., 1989. Azimuthal anisotropy in the earth from observations of SKS at GEOSCOPE and NARS broadband stations, *Bull. seism. Soc. Am.,* **79**(5), 1542–1558.

Walker, A.M. & Wookey, J., 2012. MSAT—a new toolkit for the analysis of elastic and seismic anisotropy, *Comput. Geosci.,* **49,** 81–90.

Walker, A.M., Forte, A.M., Wookey, J., Nowacki, A. & Kendall, J.-M., 2011. Elastic anisotropy of D'' predicted from global models of mantle flow, *Geochem. Geophys. Geosyst.,* **12**(10), doi:10.1029/2011GC003732.

Walker, A.M., Dobson, D.P., Wookey, J., Nowacki, A. & Forte, A.M., 2018. The anisotropic signal of topotaxy during phase transitions in D'', *Phys. Earth planet. Inter.,* **276,** 159–171.

Wang, Y. & Wen, L., 2007. Complex seismic anisotropy at the border of a very low velocity province at the base of the Earth's mantle, *J. geophys. Res.,* **112**(B9), doi:10.1029/2006JB004719.

Wirth, E.A. & Long, M.D., 2014. A contrast in anisotropy across mid-lithospheric discontinuities beneath the central United State—a relic of craton formation, *Geology,* **42**(10), 851–854.

Wolf, J., Creasy, N., Pisconti, A., Long, M.D. & Thomas, C., 2019. An investigation of seismic anisotropy in the lowermost mantle beneath Iceland, *J. geophys. Int.,* **219**(Supplement_1), S152–S166.

Wolfe, C.J. & Silver, P.G., 1998. Seismic anisotropy of oceanic upper mantle: shear wave splitting methodologies and observations, *J. geophys. Res.,* **103**(B1), 749–771.

Wookey, J. & Kendall, J.-M., 2008. Constraints on lowermost mantle mineralogy and fabric beneath Siberia from seismic anisotropy, *Earth planet. Sci. Lett.,* **275**(1-2), 32–42.

Wookey, J., Kendall, J.-M. & Rümpker, G., 2005a. Lowermost mantle anisotropy beneath the north Pacific from differential S-ScS splitting, *J. geophys. Int.,* **161**(3), 829–838.

Wookey, J., Stackhouse, S., Kendall, J.-M., Brodholt, J. & Price, G.D., 2005b. Efficacy of the post-perovskite phase as an explanation for lowermost-mantle seismic properties, *Nature,* **438**(7070), 1004–1007.

Yuan, K. & Beghein, C., 2013. Seismic anisotropy changes across upper mantle phase transitions, *Earth planet. Sci. Lett.,* **374,** 132–144.

Zhao, L. & Chevrot, S., 2011. An efficient and flexible approach to the calculation of three-dimensional full-wave Fréchet kernels for seismic tomography—II. Numerical results, *J. geophys. Int.,* **185**(2), 939–954.

SUPPORTING INFORMATION

Supplementary data are available at *GJI* online.

Figure S1. Synthetic seismograms computed for the PREM model with a HTI layer localized between 24 and 220 km plotted against the backazimuth of the incoming seismic energy. The epicentral distance is 100°. The radial component is shown in black and the transverse is shown in red. Predicted arrival time for *SKS*, *SKKS* and *ScS* are shown as the vertical orange, red and blue bars respectively.
Figure S2. Synthetic seismograms computed for the PREM model with a HTI layer localized between 24 and 220 km plotted against the backazimuth of the incoming seismic energy. The epicentral distance is 110°. The radial component is shown in black and the transverse is shown in red. Predicted arrival time for *SKS*, *SKKS* and S_{diff} are shown as the vertical orange, red and green bars, respectively.
Figure S3. Synthetic seismograms computed for the PREM model with olivine style anisotropy localized between 24 and 220 km plotted against the backazimuth of the incoming seismic energy. The epicentral distance is 100°. The radial component is shown in black and the transverse is shown in red. Predicted arrival time for *SKS*, *SKKS* and *Scs* are shown as the vertical orange, red and blue bars, respectively.
Figure S4. Synthetic seismograms computed for the PREM model with olivine style anisotropy localized between 24 and 220 km plotted against the backazimuth of the incoming seismic energy. The epicentral distance is 110°. The radial component is shown in black and the transverse is shown in red. Predicted arrival time for *SKS*, *SKKS* and S_{diff} are shown as the vertical orange, red and green bars respectively. Phases with large amplitude arriving in the 1450−1500 s range correspond to *PPPP*. For this particular symmetry class they are strongly affected by the anisotropy in the backazimuthal range 45−135°.
Figure S5. Synthetic seismograms computed for the PREM model with olivine style anisotropy localized between 24 and 220 km plotted against the backazimuth of the incoming seismic energy. The epicentral distance is 120°. The radial component is shown in black and the transverse is shown in red. Predicted arrival time for *SKS*, *SKKS* and S_{diff} are shown as the vertical orange, red and green bars, respectively. Phases with large amplitude arriving between *SKS* ans *SKKS* correspond to *PPPP*. For this particular symmetry class they are strongly affected by the anisotropy in the backazimuthal range 45−135°.
Figure S6. Synthetic seismograms computed for the PREM model bridgmanite style anisotropy localized at the base of the base of the lower mantle in a 250-km-thick D'' plotted against the backazimuth of the incoming seismic energy. The epicentral distance is 100°. The radial component is shown in black and the transverse is shown in red. Predicted arrival time for *SKS*, *SKKS* and *ScS* are shown as the vertical orange, red and blue bars respectively.
Figure S7. Synthetic seismograms computed for the PREM model a bridgmanite style anisotropy localized at the base of the base of the lower mantle in a 250-km-thick D'' plotted against the backazimuth of the incoming seismic energy. The epicentral distance is 110°. The radial component is shown in black and the transverse is shown in red. Predicted arrival time for *SKS*, *SKKS* and S_{diff} are shown as the vertical orange, red and green, respectively.
Figure S8. Synthetic seismograms computed for the PREM model bridgmanite style anisotropy localized at the base of the base of the lower mantle in a 250-km-thick D'' plotted against the backazimuth of the incoming seismic energy. The epicentral distance is 120°. The radial component is shown in black and the transverse is shown in red. Predicted arrival time for *SKS*, *SKKS* and S_{diff} are shown as the vertical orange, red and green, respectively.
Figure S9. Synthetic seismograms computed for the PREM model with post-perovskite style anisotropy localized at the base of the base of the lower mantle in a 250-km-thick D'' plotted against the backazimuth of the incoming seismic energy. The epicentral distance is 100°. The radial component is shown in black and the transverse is shown in red. Predicted arrival time for *SKS*, *SKKS* and *ScS* are shown as the vertical orange, red and blue, respectively.
Figure S10. Synthetic seismograms computed for the PREM model with post-perovskite style anisotropy localized at the base of the base of the lower mantle in a 250-km-thick D'' plotted against the backazimuth of the incoming seismic energy. The epicentral distance is 110°. The radial component is shown in black and the transverse is shown in red. Predicted arrival time for *SKS*, *SKKS* and S_{diff} are shown as the vertical orange, red and green, respectively.
Figure S11. Synthetic seismograms computed for the PREM model with post-perovskite style anisotropy localized at the base of the base of the lower mantle in a 250-km-thick D'' plotted against the backazimuth of the incoming seismic energy. The epicentral distance is 120°. The radial component is shown in black and the transverse is shown in red. Predicted arrival time for *SKS*, *SKKS* and S_{diff} are shown as the vertical orange, red and green respectively.
Figure S12. Same as Fig. 17 of the main manuscript but for the vertical component.
Figure S13. Comparison of synthetic waveforms computed by SPECFEM3D_GLOBE (black) and AxiSEM3D (dashed red) for the benchmark test presented in Section 6 of the main text. The record section shows the radial component for all the stations mapped in Fig. 15 of the main text located in the ∼90−130° range of epicentral distance.
Figure S14. Same as Fig. S13 but for the transverse component.
Figure S15. Same as Fig. S13 but for the vertical component.